

GRAIN ALIGNMENT INDUCED BY RADIATIVE TORQUES: EFFECTS OF INTERNAL RELAXATION OF ENERGY AND COMPLEX RADIATION FIELDS

THIEM HOANG & A. LAZARIAN

Dept. of Astronomy, University of Wisconsin, Madison, WI53706; hoang; lazarian@astro.wis.edu

Draft version April 23, 2022

ABSTRACT

Earlier studies of grain alignment dealt mostly with interstellar grains that have strong internal relaxation of energy which aligns grain axis of maximum moment of inertia with respect to grain's angular momentum. In this paper, we study the alignment by radiative torques for large irregular grains, e.g., grains in accretion disks, for which internal relaxation is subdominant. We use both numerical calculations and the analytical model of a helical grain introduced by us earlier. We demonstrate that grains in such a regime exhibit more complex dynamics. In particular, if initially the grain axis of maximum moment of inertia makes a small angle with angular momentum, then radiative torques can align the grain axis of maximum moment of inertia with angular momentum, and both axis of maximum moment of inertia and angular momentum are aligned with the magnetic field when attractors with high angular momentum (high- J attractors) are available. For the alignment without high- J attractors, beside the earlier studied attractors with low angular momentum (low- J attractors), there appears new low- J attractors. The former and later cases correspond to the alignment with long axes perpendicular and parallel to the angular momentum, respectively. In addition, we also study the alignment of grains in the presence of strong internal relaxation, but induced not by a radiation beam as in earlier studies, instead, induced by a complex radiation field, that can be decomposed into dipole and quadrupole components. We found that in this situation, the parameter space q^{max} , for the existence of high- J attractors in trajectory maps is more extended, which entails higher degrees of polarization expected. Our obtained results are useful for modeling polarization arising from aligned grains in molecular clouds and accretion disks.

Subject headings: Polarization -dust extinction -ISM: magnetic fields

1. INTRODUCTION

Magnetic fields play a crucial role in many astrophysical processes (e.g., star formation, accretion disks, cosmic ray transport). An important and easily available way to map magnetic fields is to observe the polarization of emission or absorption by aligned grains (Goodman et al. 1995; Hildebrand et al. 2000, 2002; Crutcher et al. 2004). The reliable interpretation of polarimetry in terms of magnetic fields requires, however, a solid understanding of the alignment of grains. This is the major motivation of work in the field of grain alignment. An additional motivation to understand when grains get aligned comes from the necessity of separating the polarization by dust grains from the polarized Cosmic Microwave Background (CMB) signal (see Lazarian 2008).

Grain alignment is a complex area of studies related to many physical effects of different time scales (see review by Lazarian 2007). It is also the research area associated with the names of Lyman Spitzer and Ed Purcell, who decisively contributed to understanding of a number of fundamental physical processes of grain alignment.

A number of mechanism has been known to induce grain alignment (see Lazarian 2007). However, recently grain helicity has been discussed as the necessary element of successful alignment. Note that the idea of grains having twist and therefore interacting differently with left and right polarized photons can be traced back to the pioneering work by Dolginov & Mytrophanov (1976). A more recent work in the area showed that a similar effect is present when irregular grains interact with a gaseous

flow (Lazarian & Hoang 2007b).¹

In this paper we concentrate on studying grain alignment by radiative torques (hereafter RATs). However, the intrinsic similarity of the radiative and mechanical torques acting on helical grains (see discussion in Lazarian & Hoang 2007b) makes our present results applicable to the alignment by mechanical torques. Note that for the alignment of helical grains, the magnetic field acts only through inducing the Larmor precession. Therefore the alignment may potentially occur with both longer and shorter grain axes perpendicular to the magnetic field. Observations of interstellar dust indicate that the alignment with the long axes perpendicular to the magnetic field is dominant in the diffuse gas. Therefore we shall call this alignment *right alignment*, and the opposite type of alignment we shall call *wrong alignment*. Different alignment processes produce either right or wrong alignment and the goal of the grain alignment theory is to predict correctly both the direction and the degree of the expected alignment.

As dust grain scatters or absorbs photons it experiences radiative torques. These torques can be stochastic or regular. Stochastic RATs arise from, for instance, a spheroidal grain randomly emitting or absorbing photons. The latter process, for instance, was invoked by Harwit (1970) in his model of grain alignment based on grains being preferentially spun up in the direction

¹ Such flows arise naturally in the reference of a grain as the grain interacts with ubiquitous MHD turbulence (Lazarian & Yan 2002; Yan & Lazarian 2003; Yan, Lazarian, & Draine 2004).

perpendicular to the photon beam. However, Purcell & Spitzer (1971) showed that the randomization arising from the same grain emitting thermal photons makes the achievable degree of grain alignment negligible. In fact, they showed that stochastic RATs arising from grain thermal emission is an important process of grain randomization. More recently, grain thermal emission was analyzed as a source of the excitation of grain rotation as well as its damping in relation to the rotation of tiny spinning grains that are likely to be responsible for the so-called anomalous foreground emission (Draine & Lazarian 1998).

RATs were first discussed by Dolginov (1972) in terms of chiral, e.g. hypothetical quartz grains. The idea is that starlight passing through such grains would spin them up. Later, Dolginov & Mytrophanov (1976) considered an irregular grain model of two spheroids twisted to each other, made of more accepted materials, e.g. silicate grains, and claimed that these grains will be both spun up and aligned by *regular RATs*. This work was, unfortunately, mostly ignored for 20 years.

Grain alignment by RATs drew much attention when Bruce Draine modified the Discrete Dipole Approximation Code (Draine & Flatau 2004, hereafter DDSCAT) and enabled later researchers to calculate RATs for irregular grains.²

Draine & Weingartner (1996, hereafter DW96) treated RATs as a kind of pinwheel torque, and they found that RATs can accelerate grains to suprathreshold rotations. Later, Draine & Weingartner (1997, hereafter DW97) introduced many essential elements of the modern treatment of RATs, for instance, phase trajectory maps. They confirmed Dolginov & Mytrophanov (1976) hypothesis that RATs can produce the alignment by their own. However, the important moments of grain dynamics, so-called crossovers, were not treated correctly in the paper. Crossovers, are special events in the dynamics of grains rotating subject to regular torques. During crossovers grain angular velocity approaches its minimal value and models of crossovers caused by pinwheel torques in Spitzer & McGlynn (1979) and in Lazarian & Draine (1997) envisaged grain flipping with the direction of the angular momentum staying the same. DW97, however, assumed that the RAT crossovers are different and during the RAT-induced crossovers angular momentum changes its direction to the opposite. This treatment of crossovers resulted in grains having cyclic trajectories, which were, in fact, an artifact of the adopted treatment, as was shown later (Lazarian & Hoang 2007a, henceforth LH07a). In fact, LH07a showed that instead of cyclic trajectories, one gets situations when RATs tend to *slow* grains down.

A more general analysis for dynamics of RAT alignment was done in Weingartner & Draine (2003, henceforth WD03), where thermal fluctuations within grain were accounted for. These fluctuations were shown by Lazarian (1994, see also Lazarian & Roberge 1997) to induce grain thermal wobbling, which amplitude gets larger as the grain angular momentum approaches its thermal values. For their choice of parameters, WD03

found that an attractor with low angular momentum, so-called, low- J attractor, appears on the trajectory phase maps.³ The study, however, was limited in terms of parameter space explored. In fact, it was a numerical study of alignment of a single grain subjected to the electromagnetic wave of a single frequency at a single incident direction. Therefore implications of the study for the problem of the RAT alignment were difficult to evaluate.

We feel that the numerical work above done with DDSCAT should be treated as an experimental attack on the problem of the RAT alignment. The limitations of such an approach are self-evident. For instance, to obtain predictions one should analyze many hundreds of different grain shapes and many wavelengths and many incident directions. The study in DW97 included 3 shapes and resulting torques looked very different, which made one wonder what causes the alignment⁴. At the same time, unfortunately, the analytical study in Dolginov & Mytrophanov (1976) was in error.

The first analytical model (henceforth AMO) of RATs consistent with the numerical calculations was proposed in LH07a. This study provided simple analytical expressions for the RATs (see also §2). In particular, the functional forms of the torques acting on grains of different shapes are similar, with the difference between the grains of different shapes amounting to a single parameter, termed q^{max} -ratio, which is the ratio of the magnitudes of two first components of torques in the grain symmetry system of reference where the radiation direction is the symmetry axis. AMO allowed theoretical predictions and the analytical treatment of the RAT alignment. As a result, studies of a parameter space seized to be an insurmountable problem. In LH07a, similar to DW97, the thermal fluctuations were intentionally disregarded and in such a setup the low- J attractors, rather than cyclic trajectories, were reported. In fact, it became clear that RATs, over a large part of the parameter space, *spin down* rather than *spin up* grains. Using AMO, LH07a obtained the values q^{max} for which grains have only low- J attractors and when they have both low- J and high- J attractors simultaneously.

AMO was extensively used in all our papers that followed. For instance, in Hoang & Lazarian (2008a, henceforth HL08a), we studied the RAT alignment in the presence of thermal fluctuations using both AMO and DDSCAT for an extended sample of grain shapes, radiation direction and wavelength. We found that *irregular* grains do not stop completely, but rotate at a rate, which is comparable with the rate of thermal rotation at the dust temperature, which agrees with an earlier example in WD03. Importantly, HL08a considered the RAT alignment in the presence of gaseous bombardment and reported a new effect, namely, the transfer between the low- J and high- J attractors, in situations when the both low- J and high- J attractors were present simultaneously⁵. Thus, counterintuitively, the collisions were

³ Conventionally, an attractor with angular momentum J larger than the thermal value is called a high- J attractor, and the attractor with J of the order of thermal value is called low- J attractor.

⁴ In relation to this one of us (AL) recalls that Lyman Spitzer after studying the work on RATs suggested that one should seek for some simple trigonometric fits to torques that would produce the alignment.

⁵ Note that the parameter space for the existence of low- J and

² The only work on RATs before that was Lazarian (1995) which corrected some of the points in the Dolginov & Mytrophanov (1976) study, but underestimated the importance of RATs.

found to *increase* the alignment.

The most important practical implication of the LH07a and HL08a studies was that, over a large range of the parameter space of q^{max} -ratio and angles between the magnetic field and radiation direction, the grains rotate thermally and therefore, as a result the aforementioned thermal fluctuations of grains, and exhibit the reduced alignment of grain axes with respect to \mathbf{J} . This opened possibilities of estimating the expected alignment and comparing it to the alignment inferred from observations. Importantly enough, Lazarian & Hoang (2008, henceforth LH08) reported, that in the presence of superparamagnetic inclusions (Jones & Spitzer 1967, Mathis 1986, Bradley 1994, Martin 1994, Goodman & Whittet 1994), the high- J attractors *always* exist. This finding entails a very non-trivial effect, namely, that, in the presence of both superparamagnetic inclusions, grains, that otherwise would rotate subthermally, get into the state of fast suprathreshold rotation. According to HL08a, this also means that *all* grains eventually get into the state of fast rotation and *perfect* alignment. From the point of view of observations, this opens prospects of testing the existence of superparamagnetic inclusions by measuring the degree of polarization.

This paper continues our studies in LH07a and HL08a. The major issues we address below are (1) the effect of internal relaxation, and (2) the effect of complex radiation field on the grain alignment.

The first issue is important in terms of the alignment of large grains, e.g. grains within proto-planetary accretion disks. The alignment of such grains was assumed in a recent modeling of polarization from T-Tauri accretion disks in Cho & Lazarian (2007). Grains which are important for such a modeling may, however, should be sufficiently large that the internal relaxation time for them is longer than the alignment time. Therefore, how grains get aligned in the absence of efficient internal relaxation is an important question.

The second issue is vital for modeling the polarization from both disks and dark clouds. The latter modeling which used the RAT alignment was undertaken in Cho & Lazarian (2005), Pelkonen et al. (2007) and Bethell et al. (2007). All these studies assumed rather naive models of alignment. In particular, the actual modeling would require taking into account the actual complex radiation field that is being experienced by the grain, rather than to assume that the radiation is coming from a point source.

In what follows, in §2 we briefly describe the AMO, grain torque-free motion, and calculations of RATs. In §3 we compare the Barnett and nuclear relaxation times with the radiative alignment time and identify grain size when the internal relaxation can be disregarded. In §4 we study the properties of RATs and the resulting RAT alignment for large grains in the absence of the internal relaxation. Grain alignment by RATs arising from dipole and quadrupole components of radiation fields is studied in §5. We discuss our findings in §6, and our summary is presented in §7.

2. RADIATIVE TORQUES

2.1. Definition of radiative torques

high- J attractors are similar and known through the LH07a study.

Considering only the anisotropic component of the radiation field, the radiative torque resulting from the interaction of a radiation beam with a grain is then defined by

$$\mathbf{\Gamma}_{rad} = \frac{u_{rad} a^2 \bar{\lambda}}{2} \gamma \overline{\mathbf{Q}}_{\Gamma}(\Theta, \beta, \Phi), \quad (1)$$

where a is the grain size, γ is the degree of anisotropy, $\bar{\lambda}$ and u_{rad} are the mean wave length and total energy density of the radiation field, respectively; \mathbf{Q}_{Γ} is the RAT efficiency vector depending on angles Θ, β and Φ , and its overline denotes averaging over the spectrum of radiation field (DW96); Θ is the angle between the axis of maximum moment of inertia \mathbf{a}_1 and the radiation direction \mathbf{k} , β is the rotation angle about \mathbf{a}_1 and Φ is the precession angle of \mathbf{a}_1 about \mathbf{k} (see Fig. 1*upper*). In the lab coordinate system $\hat{\mathbf{e}}_1 \hat{\mathbf{e}}_2 \hat{\mathbf{e}}_3$, \mathbf{Q}_{Γ} is decomposed as

$$\mathbf{Q}_{\Gamma}(\Theta, \beta, \Phi) = Q_{e_1}(\Theta, \beta, \Phi) \hat{\mathbf{e}}_1 + Q_{e_2}(\Theta, \beta, \Phi) \hat{\mathbf{e}}_2 + Q_{e_3}(\Theta, \beta, \Phi) \hat{\mathbf{e}}_3. \quad (2)$$

2.2. Analytical model of RATs

LH07a proposed an analytical model of RATs arising from the interaction of a helical grain, consisting of a mirror attached to an ellipsoid body with a radiation beam. Although this model was derived in the geometric optics approximation, LH07a proved that it represents well RATs obtained by DDSCAT.

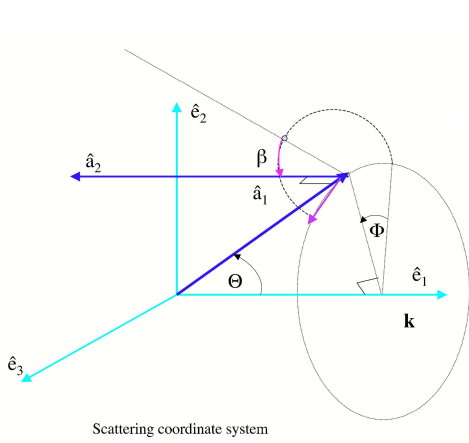
The geometry of AMO is depicted in Figure 2. It has a weightless mirror tilted by an angle α about the axis \mathbf{a}_2 attached to an ellipsoid. Detail comparisons of RATs on the model and irregular grains suggested $\alpha = \pi/4$. For a given direction of the grain with respect to the radiation direction \mathbf{k} , RATs arising from the scattering of photons on the mirror are functions of the angles Θ, β and Φ . LH07a calculated three components of RATs at $\Phi = 0$: $Q_{e_1}(\Theta, \beta, 0)$, $Q_{e_2}(\Theta, \beta, 0)$ and $Q_{e_3}(\Theta, \beta, 0)$.

LH07a found that whether the RAT alignment has high- J or low- J attractors depends on the ratio of torque components $q^{max} = Q_{e_1}^{max}/Q_{e_2}^{max}$ (see Appendix A). Therefore, this parameter has been used to characterize the RAT alignment in LH07a. For irregular grains, LH07a found that q^{max} depends on the wavelength of radiation, grain shape, size and composition, ranging from 10^{-3} to 10^2 . Thus, we treat q^{max} as a variable parameter in this paper.

To conform with numerical calculations using DDSCAT, we combine the functional forms of RATs from AMO with the scaling for the magnitude of RATs as a function of wavelength and grain size. The final RATs used in our series of papers are given in Appendix A. We note that for the AMO, the functional forms of RATs do not depend on wavelength, so that we can simplify the notations by using \mathbf{Q}_{Γ} instead of $\overline{\mathbf{Q}}_{\Gamma}$.

2.3. Torque-free motion

The motion of a triaxial grain in the absence of external torques, namely, torque-free motion, is well-known (see Landau & Lifshitz 1976; also WD03). Let consider an irregular grain with angular momentum J , and rotational energy E . It is convenient to introduce a dimensionless



Scattering coordinate system

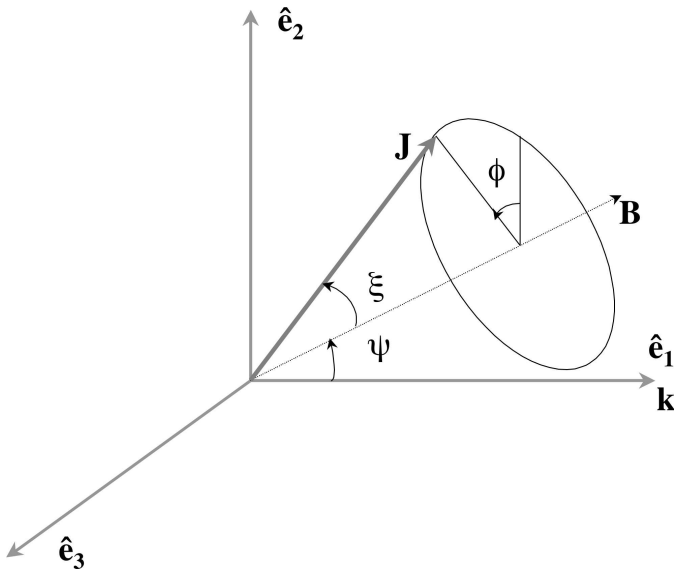


FIG. 1.— *Upper panel:* Orientation of a grain, described by three principal axes \hat{a}_1, \hat{a}_2 and \hat{a}_3 , in the lab coordinate system $\hat{e}_1, \hat{e}_2, \hat{e}_3$ is defined by three angles Θ, β and Φ . The direction of incident radiation beam \mathbf{k} is along \hat{e}_1 . *Lower panel:* The orientation of angular momentum \mathbf{J} in the lab coordinate system, ψ is the angle between the magnetic field \mathbf{B} and \mathbf{k} , ξ is the angle between \mathbf{J} and \mathbf{B} , and ϕ is the Larmor precession angle of \mathbf{J} about \mathbf{B} .

parameter⁶

$$p = \frac{2I_1 E}{J^2}, \quad (3)$$

where I_1 is the inertia moment about the axis of maximum moment of inertia \mathbf{a}_1 , and other inertia moments are smaller than I_1 , i.e., $I_1 > I_2 > I_3$. Here p spans in the range 1 to I_1/I_3 , where the lower and upper limits correspond to the grain rotation about the axis of maximum moment of inertia \mathbf{a}_1 and axis of minimum moment of inertia \mathbf{a}_3 , respectively.

For the torque-free motion, the angular velocity components about the three principal axes, ω_1, ω_2 and ω_3 can be obtained analytically as functions of p and time t (see WD03; HL08a for their expressions). In Figure 3 we plot ω_1, ω_2 and ω_3 as functions of time t/P_t with P_t being the

⁶ This parameter was denoted by q in WD03, however, we use p to avoid the possible confusion with q^{max} .

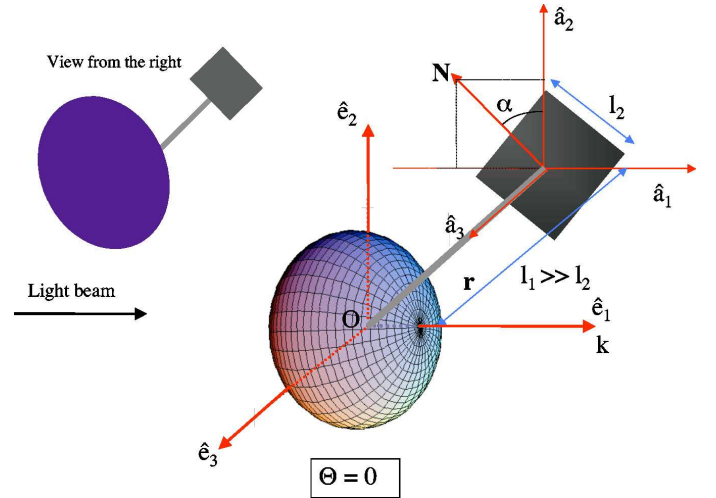


FIG. 2.— Sketch of an AMO consisting of a weightless mirror attached to a perfectly reflecting ellipsoid. Principal axes \hat{a}_1, \hat{a}_2 and \hat{a}_3 define a body coordinate system, and \hat{e}_1, \hat{e}_2 and \hat{e}_3 define the lab coordinate system. Θ is the angle between \hat{a}_1 and the radiation direction $\mathbf{k} \parallel \hat{e}_1$. \mathbf{N} is the normal vector lying in the plane $\hat{a}_2\hat{a}_3$, and α is the tilted angle of the mirror in the body coordinate system. \mathbf{r} is the radius vector of length l_1 connecting the ellipsoid to the mirror, l_2 is the mirror size and $l_1 \gg l_2$ is assumed.

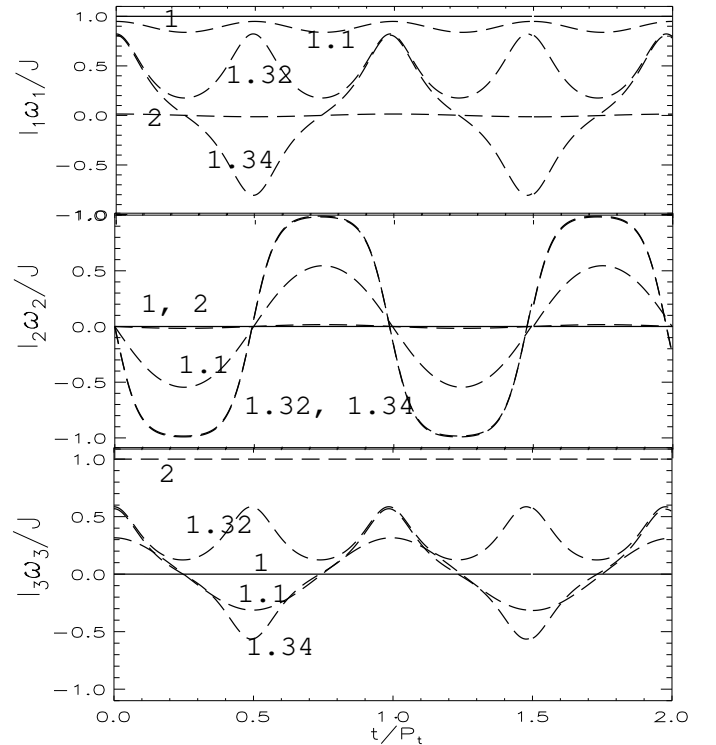


FIG. 3.— Angular velocity components as functions of time t/P_t with P_t being the rotation period, for different values of p for an irregular grain with $I_1 : I_2 : I_3 = 2 : 1.5 : 1$ and in a positive flipping state, i.e., ω_1 and ω_3 both being positive for $p < I_1/I_2$. The value of p corresponding to each curve is labelled.

rotation period, for different p for an irregular grain with ratio of inertia moments $I_1 : I_2 : I_3 = 2 : 1.5 : 1$. The plot corresponds to a positive flipping state, i.e., ω_1 and ω_3 are both positive for $p < I_1/I_2$. Similarly, when ω_1 and ω_3 are both negative for $p < I_1/I_2$, we call negative flipping state (see HL08a for details).

We can see that when $p \rightarrow 1$ or $I_1/I_3 = 2$, the rotation is stable about \mathbf{a}_1 and \mathbf{a}_3 axes, respectively. However, the rotation is not stable about the intermediate axis \mathbf{a}_2 when $p = 1.32$ and 1.34 , which are very close to $I_1/I_2 = 1.333$. In fact, the middle panel shows that as $p \rightarrow I_1/I_2$, the grain gets into a negative state with $I_2\omega_2/J = -1$ for almost one half period, and then reverses its rotational state, staying there for another half period. Of course, at $p = I_1/I_2$, we have $I_2\omega_2/J = 1$ and $\omega_1 = \omega_3 = 0$.

Because the timescale of torque-free motion is much shorter than the internal relaxation timescale and other dynamical timescales (e.g., Larmor precession, gas damping times), we can average RATs over such a motion to obtain $\tilde{Q}_\Gamma(\Theta, \beta, \Phi)$ where the tilde denotes averaging over torque-free motion. Resulting RATs are functions of ξ, ϕ, ψ, p and J .

2.4. Radiative torques in alignment coordinate system

To study the alignment of the angular momentum \mathbf{J} with the magnetic field \mathbf{B} , we represent RATs in the spherical coordinate system J, ξ, ϕ , the so-called alignment coordinate system (see the lower panel in Fig. 1).

In this alignment coordinate system, the RAT $\mathbf{\Gamma}_{rad}$ can be written as

$$\mathbf{\Gamma}_{rad} = M[F(\xi, \phi, p, J)\hat{\xi} + G(\xi, \phi, p, J)\hat{\phi} + H(\xi, \phi, p, J)\hat{\mathbf{J}}] \quad (4)$$

where the dependence on the angle between the radiation direction \mathbf{k} and \mathbf{B} , ψ , is omitted,

$$M = \frac{\gamma u_{rad} a^2 \bar{\lambda}}{2}, \quad (5)$$

F , which is the torque component parallel to $\hat{\xi}$, acts to change the orientation of \mathbf{J} with respect to \mathbf{B} . H , the component parallel to $\hat{\mathbf{J}}$, is to spin grains up and G induces the precession of \mathbf{J} about the magnetic field or radiation. The later are given by

$$\begin{aligned} H(\xi, \phi, p, J) &= \tilde{Q}_{e_1}(\xi, \phi, p, J)(\cos \psi \cos \xi - \sin \psi \sin \xi \cos \phi) \\ &\quad + \tilde{Q}_{e_2}(\xi, \phi, p, J)(\sin \psi \cos \xi + \cos \psi \sin \xi \cos \phi) \\ &\quad + \tilde{Q}_{e_3}(\xi, \phi, p, J) \sin \xi \sin \phi, \end{aligned} \quad (6)$$

$$\begin{aligned} F(\xi, \phi, p, J) &= \tilde{Q}_{e_1}(\xi, \phi, p, J)(-\sin \psi \cos \xi \cos \phi - \sin \xi \cos \psi) \\ &\quad + \tilde{Q}_{e_2}(\xi, \phi, p, J)(\cos \psi \cos \xi \cos \phi - \sin \xi \sin \psi) \\ &\quad + \tilde{Q}_{e_3}(\xi, \phi, p, J) \cos \xi \sin \phi, \end{aligned} \quad (7)$$

where ξ, ψ and ϕ are angles describing the direction of \mathbf{J} in the lab coordinate system (see Fig. 1, lower panel). Here $\tilde{Q}_{e_i}(\xi, \phi, p, J)$ with $i = 1, 2$ and 3 are RAT components along \mathbf{e}_i axes, respectively, obtained by averaging Q_{e_i} over torque-free motion.

We define also the torque components along grain axes $\mathbf{a}_1, \mathbf{a}_2$ and \mathbf{a}_3 as

$$Q_{a_i}(\xi, \phi, p, J) = \mathbf{Q}_\Gamma \cdot \mathbf{a}_i \text{ for } i=1 \text{ to } 3, \quad (8)$$

and thus, the work done by RATs per second

$$Q_\omega = \mathbf{Q}_\Gamma \cdot \boldsymbol{\omega} = Q_{a_1}\omega_1 + Q_{a_2}\omega_2 + Q_{a_3}\omega_3. \quad (9)$$

Here ω_i for $i = 1, 2$ and 3 corresponds to the components of angular velocity along three grain axes \mathbf{a}_i . Their expressions for torque-free motion are given in Appendix

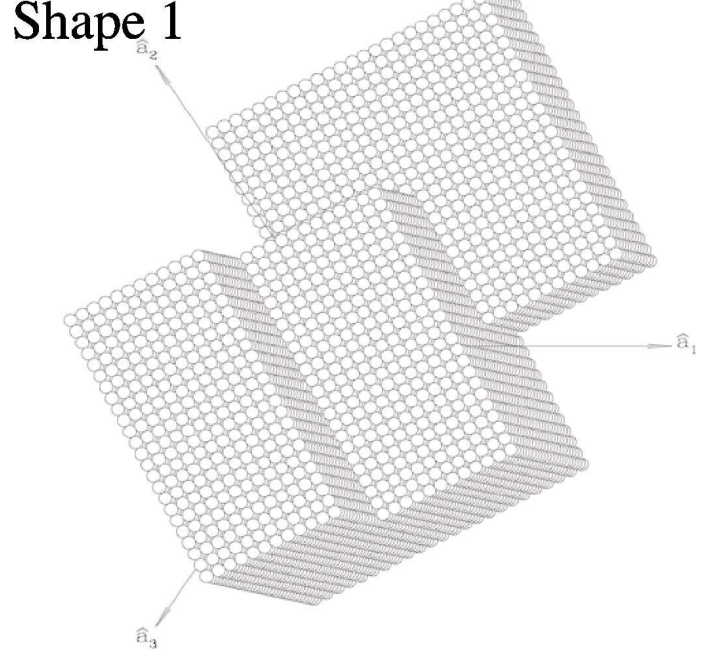


FIG. 4.— Sketch of the irregular grain, shape 1, built from 13 cubes adopted in our calculations. The inertia moments along principal axes are $I_1 : I_2 : I_3 = 1.745 : 1.61 : 0.876$. A of HL08a. In addition, from Figure 1, we have

$$\mathbf{a}_1 = \mathbf{e}_1 \cos \Theta + \mathbf{e}_2 \sin \Theta \cos \Phi + \mathbf{e}_3 \sin \Theta \sin \Phi, \quad (10)$$

$$\begin{aligned} \mathbf{a}_2 &= -\mathbf{e}_1 \sin \Theta \cos \beta + \mathbf{e}_2 (\cos \Theta \cos \Phi \cos \beta - \sin \Phi \sin \beta) \\ &\quad + \mathbf{e}_3 (\cos \Theta \sin \Phi \cos \beta + \cos \Phi \sin \beta), \end{aligned} \quad (11)$$

$$\begin{aligned} \mathbf{a}_3 &= \mathbf{e}_1 \sin \Theta \sin \beta - \mathbf{e}_2 (\cos \Theta \cos \Phi \sin \beta + \sin \Phi \cos \beta) \\ &\quad + \mathbf{e}_3 (-\cos \Theta \sin \Phi \sin \beta + \cos \Phi \cos \beta). \end{aligned} \quad (12)$$

2.5. Calculations of RATs

Taking analytical expressions $Q_{e_i}(\Theta, \beta, \Phi = 0)$ with $i = 1, 2$ and 3 from AMO (see Appendix A), we first calculate $Q_{e_i}(\Theta, \beta, \Phi)$ by using equations (A13)-(A15) for $\Theta \in [0, \pi]$, $\beta \in [0, 2\pi]$, and $\Phi \in [0, 2\pi]$. Next, we calculate RATs for J from 0.1 to $20I_1\omega_T$, ξ from 0 to π , ϕ from 0 to 2π , and p from 1 to I_1/I_3 and for a given light direction ψ . For a given set of parameters J, ξ, ϕ, p , we use coordinate transformations to get angles Θ, β and Φ as functions of Euler angles (see Appendix A in HL08a). Finally, torque components $Q_{e_i}(\xi, \psi, \phi)$ are obtained using interpolation for $Q_{e_i}(\Theta, \beta, \Phi)$. Then we average $Q_{e_i}(\xi, \psi, \phi)$ over Euler angles, i.e., averaging over torque-free motion, to get $\tilde{Q}_{e_i}(\xi, \psi, \phi)$.

Substituting $\tilde{Q}_{e_i}(\xi, \psi, \phi)$ into equations (6), (7) and (9) we obtain $F(\xi, \psi, \phi), H(\xi, \psi, \phi)$ and $Q_\omega(\xi, \psi, \phi)$. We then average them over angle ϕ to get the Larmor precession averaged values. Since these torques are functions of J, ξ, p , we denote them by $\langle F \rangle_\phi(J, \xi, p), \langle H \rangle_\phi(J, \xi, p)$ and $\langle Q_\omega \rangle_\phi(J, \xi, p)$, where the dependence on ψ is omitted. We will use these results to solve equations of motion for the alignment in §4.

3. TIME SCALES: GAS DAMPING, INTERNAL RELAXATION AND RADIATIVE ALIGNMENT

3.1. Gas damping time

We represent the magnitude of torques in terms of the thermal angular momentum, and the gas damping time.

The later, for the sake of simplicity, can be obtained for an oblate spheroid, with the moments of inertia $I_{\parallel} = I_1, I_{\perp} = I_2 = I_3$.⁷ The expressions for triaxial ellipsoids are more complex, but do not change results substantially. Then, the thermal angular momentum is given by

$$J_{th} = \sqrt{I_{\parallel} k_B T_{gas}} = \sqrt{\frac{8\pi\rho a^5 s}{15} k_B T_{gas}},$$

$$= 5.89 \times 10^{-20} a_{-5}^{5/2} \hat{s}^{1/2} \hat{\rho}^{1/2} \hat{T}_{gas}^{1/2}, \quad (13)$$

with ρ density of material within the grain and $\hat{\rho} = \rho/3 \text{ g cm}^{-3}$, a grain size, $a_{-5} = a/10^{-5} \text{ cm}$, $\hat{s} = s/0.5$ with $s = b/a$ and T_{gas} gas temperature and $\hat{T}_{gas} = T_{gas}/100\text{K}$. And the damping time due to gas collision (see Roberge, DeGraff & Flatherty 1993, hereafter RDF93) is

$$t_{gas} = \frac{3}{4\sqrt{\pi}} \frac{I_{\parallel}}{n_H m_H a^4 v_{th} \Gamma_{\parallel}},$$

$$= 2.3 \times 10^{12} a_{-5} \hat{s} \hat{T}_{gas}^{-1/2} \left(\frac{30 \text{ cm}^{-3}}{n_H} \right) \text{ s}, \quad (14)$$

where v_{th} is the thermal velocity of a gas particle with density n_H , m_H is the hydrogen mass, Γ_{\parallel} is the geometrical parameter which is unity for sphere (see RDF93), and we adopted standard parameters in the ISM (see Table 1 in HL08a).

3.2. Internal relaxation timescales

A rotating paramagnetic grain experiences internal dissipation of energy due to Barnett and nuclear relaxation (see Purcell 1979 and Lazarian & Drain 1999b, hereafter LD99b, respectively). In addition, superparamagnetic inclusions can increase significantly the rate of internal relaxation (Lazarian & Hoang 2008).

Disregarding other relaxation processes within the grain, e.g., inelastic relaxation (Purcell 1979; Lazarian & Efroimsky 1998) as well as the relaxation due to superparamagnetic inclusions, the internal relaxation rate arising from Barnett and nuclear relaxation for a brick of $2a \times 2a \times 2b$ sides (see Fig. 18, lower panel) is then

$$t_{int}^{-1} \approx t_{Bar}^{-1} + t_{nucl}^{-1},$$

$$= 1.310^{-7} \hat{\rho}^{-2} \hat{s} [0.5 + 0.125 \hat{s}^2]^2 a_{-5}^{-7} \hat{s} \hat{T}_{gas} \hat{T}_d^{-1}$$

$$\times \left(\frac{J}{I_1 \omega_T} \right)^2 (h-1) f(J). \quad (15)$$

Here the Barnett and nuclear relaxation times t_{Bar} and t_{nucl} are taken from Hoang & Lazarian (2008b; HL08b), $s = b/a$, $h = I_{\parallel}/I_{\perp}$, $\omega_T = (2kT_{gas}/I_1)^{1/2}$ is the thermal angular velocity of grain at the gas temperature T_{gas} , $\hat{T}_d = T_d/15\text{K}$ with T_d being the dust temperature, and

$$f(J) = 1.610^5 [1 + \left(\frac{\omega_1 \tau_n}{2} \right)^2]^{-2} + 0.47 [1 + \left(\frac{\omega_1 \tau_{el}}{2} \right)^2]^{-1} \quad (16)$$

⁷ For the oblate spheroid with major and minor axes a and b , $I_{\parallel} = 2Ma^2/5 = (8\pi\rho/15)ba^4$, and $I_{\perp} = (4\pi\rho/15)a^2b(a^2 + b^2)$, but sometimes we define the equivalent sphere with the same volume of the grain, and use $I_i = (8\pi/15)\rho\alpha_i a^5$ with α_i for $i = 1, 2$ and 3 being dimensionless factors (see WD03).

For grains larger than $1\mu\text{m}$, $f(J) \approx 1.6 \times 10^5$ for $J = J_{th}$. In above equations, $\omega_1 = J \cos\theta / I_{\parallel}$, and τ_n is given by

$$\tau_n = 1/(\tau_{ne}^{-1} + \tau_{nn}^{-1}) \quad (17)$$

where $\tau_{ne} = 3 \times 10^{-4} (2.7/g_n)^2 (10^{22} \text{ cm}^{-3}/n_e) \text{ s}$ and $\tau_{nn} = \hbar/(3.8g_n n_n \mu_n) \approx 0.58 \tau_{ne} (n_e/n_n)$ with electron and nucleus density n_e and n_n are the relaxation time of interaction nucleus-electron and nucleus-nucleus spins, respectively. Also, $\tau_{el} = 2.9 \times 10^{-11} \text{ s}$ is the spin-spin relaxation time of electronic spins, and $\cos\theta = 1/2$ is chosen (see LD99b; HL08b)

3.3. Radiative alignment timescale

The characteristic timescale for RATs to accelerate the grain from $J = 0$ to $J = I_1 \omega$ is estimated by

$$t_{rad} = \frac{I_1 \omega}{\Gamma_{rad}} = \frac{I_1 \omega}{M \langle H \rangle_{\phi}}, \quad (18)$$

where $\langle H \rangle_{\phi}$ is the spin-up component of RATs, that is averaged over the torque-free motion and the precession angle ϕ using equation (6).

Using M given by equation (5) and $I_1 = 16\rho a^5 s/3$ for the brick of $2a \times 2a \times 2b$ sides, we obtain

$$t_{rad} = \frac{2^{3/2} (16\rho k T_{gas}/3)^{1/2} a^{1/2} s^{1/2}}{\lambda u_{rad} \gamma \langle H \rangle_{\phi}}. \quad (19)$$

For standard parameters of the ISM, it yields

$$t_{rad} \approx 2.8 \times 10^{10} \hat{\rho} \hat{T}_{gas} \hat{s} a_{-5}^{1/2} \frac{1.2 \mu\text{m}}{\lambda} \frac{u_{ISRF}}{u_{rad}} \frac{10^{-3}}{\gamma \langle H \rangle_{\phi}} \quad (20)$$

where $\hat{s} = s/0.5$ with $s = b/a$ being the ratio of long to short axes, u_{ISRF} is the energy density of interstellar radiation field (hereafter ISRF; see Mathis, Mezger, & Panagia 1983).

3.4. Radiative alignment time versus internal relaxation time

To compare the effect of RATs and internal relaxation, let us estimate the ratio of their timescales. Following equations (15) and (20) we obtain for a brick grain

$$\frac{t_{rad}}{t_{int}} = 3.7 \times 10^3 \hat{\rho}^{-1.5} [0.5 + 0.125 \hat{s}^2]^2 a_{-5}^{-6.5} \frac{\hat{T}_{gas}^{1.5}}{\hat{T}_d} \frac{1}{\hat{u}_{rad} \hat{\lambda}}$$

$$\times \frac{10^{-3}}{\gamma \langle H \rangle_{\phi}} \left(\frac{\omega}{\omega_T} \right)^3 f(J), \quad (21)$$

Here $\hat{T}_d = T_d/15\text{K}$, $\hat{u}_{rad} = u_{rad}/u_{ISRF}$, and $\hat{\lambda} = \bar{\lambda}/1.2 \mu\text{m}$. $u_{ISRF} = 8.64 \times 10^{-13} \text{ erg cm}^{-3}$ is the energy density of interstellar radiation field (hereafter ISRF; see Mathis, Mezger & Panagia 1983), and $\gamma = 0.1$.

Using the scaling of RAT magnitude obtained in LH07a: $\langle H \rangle_{\phi} \approx |Q_{\Gamma}| \approx 0.4 \left(\frac{\bar{\lambda}}{a} \right)^{-3}$ for $\bar{\lambda} > 1.8a$. We get

$$\frac{t_{rad}}{t_{int}} = 8.4 \times 10^5 \hat{\rho}^{-1.5} [0.5 + 0.125 \hat{s}^2]^2 \hat{a}_{-5}^{-9.5} \frac{\hat{T}_{gas}^{1.5}}{\hat{T}_d} \frac{\hat{\lambda}^2}{\hat{u}_{rad}}$$

$$\times \left(\frac{\omega}{\omega_T} \right)^3 f(J). \quad (22)$$

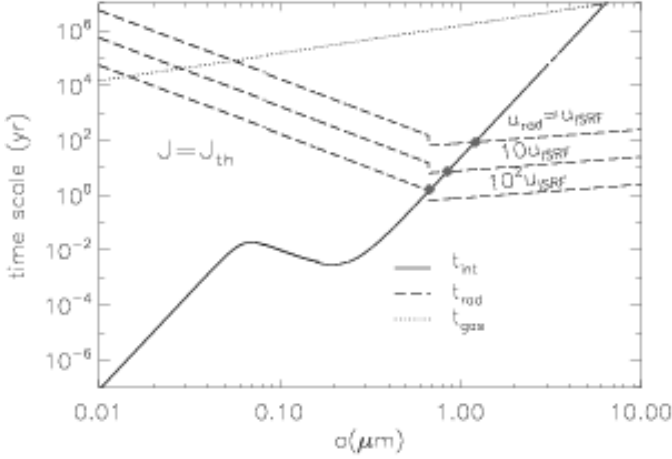


FIG. 5.— Timescales as functions of grain size for internal relaxation (t_{int}), radiative (t_{rad}) and gas damping (t_{gas}) calculated for $J = J_{th}$ and the ISM. Filled circles denote where $t_{int} = t_{rad}$.

For $\bar{\lambda} < 1.8a$, $\langle H \rangle_\phi \sim 0.4$,

$$\frac{t_{rad}}{t_{int}} = 70\hat{\rho}^{-1.5}\hat{s}\hat{a}_{-5}^{-6.5}\frac{\hat{T}_{gas}^{1.5}}{\hat{T}_d}\frac{1}{\hat{u}_{rad}\hat{\lambda}}\left(\frac{\omega}{\omega_T}\right)^3 f(J). \quad (23)$$

Both the increase of the grain size and the radiation intensity lead to the decrease of t_{rad} .

For a grain size $a = 1.2 \mu\text{m}$, $f(J = J_{th}) \sim 10^5$, so it can be seen from equation (23) that $t_{rad}/t_{int} \sim 0.67$ for the ISRF (see also Fig. 5).

Figure 5 shows t_{gas} , t_{int} and t_{rad} as functions of a for the ISM obtained from equations (14), (15) and (20), respectively. It can be seen that for grains smaller than $\sim 1 \mu\text{m}$, $t_{int}/t_{rad} \ll 1$, and decreases steeply with a decreasing. For grains larger than $\sim 1.2 \mu\text{m}$, we see that $t_{int}/t_{rad} > 1$, and t_{int}/t_{rad} increases rapidly with a . When the mean energy density u_{rad} increases by 10^2 time, the size corresponding to $t_{int} = t_{rad}$ decreases from 1.5 to $0.6 \mu\text{m}$.

Note that earlier works on grain alignment dealt with the alignment of interstellar grains with size in the range from 0.005 to $0.25 \mu\text{m}$. For this range of grain size, internal relaxation is very strong, so that the average of RATs over thermal fluctuations arising from internal relaxation was accounted for (WD03; HL08a). In some circumstances, e.g. accretion disks, molecular clouds, where larger grains corresponding to weak internal relaxation are expected, we need to study the internal and external alignment at the same time.

Another characteristic timescale involving in the grain dynamics is the Larmor precession time of grain magnetic moment about an ambient magnetic field. Due to the Barnett effect, a rotating paramagnetic grain develops a magnetic moment μ_{Bar} which is proportional to the angular velocity (see Dolginov & Myrtraphanov 1976). The value of μ_{Bar} is given by

$$\mu_{Bar} = \frac{\chi(0)V\hbar}{g\mu_B}\omega, \quad (24)$$

where $\chi(0) = 4.2 \times 10^{-2} f_p \hat{T}_d^{-1}$ with f_p being the fraction of paramagnetic material, is the magnetic susceptibility at zero frequency, V is the volume, g is gyromagnetic ration, which is ~ 2 for electrons, and $\mu_B = e/2m_e$ is the Bohr magneton.

The Larmor precession time in an external magnetic field B is then

$$t_L = \frac{2\pi I_1 \omega}{\mu_{Bar} B} \approx 4.2 \times 10^5 a_{-5}^2 \frac{\hat{\rho} \hat{T}_d}{\hat{B} \hat{\chi}(0)} \text{ s}, \quad (25)$$

where $\hat{B} = B/(5\mu\text{G})$ and $\hat{\chi}(0) = \chi(0)/10^{-3}$, and we used $I_1 = 8\pi\rho a^5/15$ for inertia moment.

It is easy to see that this time scale is shorter than both internal relaxation and radiative alignment timescales for grains larger than about μm (see Fig. 5), so that we can average RATs over the Larmor precession while dealing with the overall alignment.

4. RAT ALIGNMENT IN THE ABSENCE OF INTERNAL RELAXATION

Now let us study grain dynamics for grains larger than $1 \mu\text{m}$ in the diffuse interstellar medium. For this range of grain size, $t_{int} > t_{rad}$, the influence of internal relaxation to grain alignment can be disregarded. As a result, we follow both the evolution of angular momentum and grain axes subject to RATs.

4.1. Equations of motion

The orientation of \mathbf{J} with respect to the magnetic field \mathbf{B} is described by the following equation

$$\frac{d\mathbf{J}}{dt} = \mathbf{\Gamma}_{rad} - \frac{\mathbf{J}}{t_{gas}}, \quad (26)$$

where $\mathbf{\Gamma}_{rad}$ is the vector of radiative torque (see eq. A1), t_{gas} is the gas damping time.

With the use of equation (4), we can rewrite equation (26) in the spherical coordinate system J, ξ, ϕ , assuming that both precession timescales of \mathbf{a}_1 around \mathbf{J} and \mathbf{J} around \mathbf{B} are smaller than the internal relaxation time:

$$\frac{dJ}{dt} = M(\langle H(J, \xi, p) \rangle_\phi) - \frac{J}{t_{gas}}, \quad (27)$$

$$\frac{d\xi}{dt} = \frac{M}{J} \langle F(J, \xi, p) \rangle_\phi, \quad (28)$$

where $\langle H(J, \xi, p) \rangle_\phi$ and $\langle F(J, \xi, p) \rangle_\phi$ are spin-up and aligning components, respectively, obtained from averaging equation (6) and (7) over torque-free motion, and the precession angle ϕ and M is given by equation (5). Also, we assume that the gas damping is isotropic, and we disregard the alignment by paramagnetic dissipation.

Unlike the axisymmetric grains where the angle θ between \mathbf{a}_1 and \mathbf{J} is constant during torque-free motion, irregular grains exhibit the torque-free wobbling, and the conserved quantities are E , the total energy and J , the value of angular momentum. Therefore, for an irregular grain, similar to WD03, we can use p to describe the dynamical evolution of grain axes. With the use of equation (3), and taking time derivative of p we obtain

$$\begin{aligned} \frac{J^2 dp}{dt} &= M [I_1 \langle Q_\omega(J, \xi, p) \rangle_\phi - pJ \langle H(J, \xi, p) \rangle_\phi] \\ &\quad - \frac{J(p-1)}{t_{int}} \left(\frac{1-pI_3/I_1}{1-I_3/I_1} \right), \end{aligned} \quad (29)$$

where $\langle Q_\omega \rangle$ is the average of torque component along the angular velocity given by equation (9), and t_{int} is given

by equation (15) (see Appendix B). Let us define,

$$\langle K(J, \xi, p) \rangle_\phi = \langle Q_\omega(J, \xi, p) \rangle_\phi / (pJ), \quad (30)$$

then, equation (29) becomes

$$\frac{Jdp}{dt} = Mp[\langle K(J, \xi, p) \rangle_\phi - \langle H(J, \xi, p) \rangle_\phi] - \frac{(p-1)}{t_{int}} \left(\frac{1-pI_3/I_1}{1-I_3/I_1} \right), \quad (31)$$

Before studying grain dynamics induced by RATs, we first want to consider how the torque components $\langle F(J, \xi, p) \rangle_\phi$, $\langle H(J, \xi, p) \rangle_\phi$ and $\langle K(J, \xi, p) \rangle_\phi$ change with p and ξ . We adopt AMO that has the inertial property of triaxial ellipsoids with ratio of inertia moments $I_1 : I_2 : I_3 = 2 : 1.5 : 1$ and $I_1 : I_2 : I_3 = 1.745 : 1.610 : 0.8761$. The later is identical with the ratio of inertia moments of the shape 1 (see Fig. 4) and naturally the parameter q^{max} can be changed for the AMO (LH07a). A $1.5\mu\text{m}$ grain size and interstellar radiation field are adopted in this section.

4.2. Variation of RATs with p : stationary points for p

In Figure 6 we plot $\langle H(J, \xi, p) \rangle_\phi$ and $\langle K(J, \xi, p) \rangle_\phi$ as functions of p for $J = 10I_1\omega_T$, $\xi = 22^\circ$, 140° and $\psi = 0^\circ$ (upper panel) and 70° (lower panel) for the AMO with parameter $q^{max} = 1.2$.

We see that $\langle H(J, \xi, p) \rangle_\phi$ and $\langle K(J, \xi, p) \rangle_\phi$ decrease as p increases to I_1/I_2 , and then increase as p increases to I_1/I_3 . This is because as $p \rightarrow I_1/I_2$, grain axes wobble more rigorously about \mathbf{J} , which results in the decrease of torques due to averaging over wobbling with large amplitude. As p increases again, ω gets rotating stably about \mathbf{a}_3 , and averaged torques increase because the wobbling amplitude decreases.

In addition, $\langle H(J, \xi, p) \rangle_\phi$ and $\langle K(J, \xi, p) \rangle_\phi$ are identical at $p = 1$, $I_1/I_2 = 1.33$ and $I_1/I_3 = 2$. This arises from the fact that at these points, ω parallel to \mathbf{J} , so the projection of RATs onto \mathbf{J} , $\langle H(J, \xi, p) \rangle_\phi$, is the same with that on ω , $\langle K(J, \xi, p) \rangle_\phi$.

The sharp decrease of $\langle K(J, \xi, p) \rangle_\phi$ when $p \rightarrow I_1/I_2$ is associated with the dynamics of a triaxial ellipsoid. Nevertheless, for p very close to I_1/I_2 , ω oscillates in the lab system, and gives rise to a sharp change of $\langle K(J, \xi, p) \rangle_\phi$ (see dashed lines in Fig. 6).

Equation (31) shows that stationary points occur when $dp/dt = 0$. In the absence of internal relaxation for large grains, it requires $\langle K(J, \xi, p) \rangle_\phi - \langle H(J, \xi, p) \rangle_\phi = 0$.

Figure 7 shows $\langle K(J, \xi, p) \rangle_\phi - \langle H(J, \xi, p) \rangle_\phi$ for the same AMO with $q^{max} = 1.2$, $\psi = 0^\circ, 70^\circ$ (upper) and 2.5 , $\psi = 0^\circ$ (lower). There we omit the dependence of torques on J and ξ . We remind the reader that these cases correspond to the alignment without and with high- J attractors, respectively, when the perfect internal alignment of \mathbf{a}_1 with \mathbf{J} was assumed (see LH07a). In the upper panel, corresponding to the alignment without high- J attractors, there are three stationary points 1, 2 and 3. Let p_1 , p_2 and p_3 be the value of p at these points. It is easy to see that $p_1 = 1$, $p_2 = I_1/I_2$ and $p_3 = I_1/I_3$. In the alignment with high- J attractors (see lower panel), there exists another stationary point 4, and its value of p is denoted by p_4 . Our calculations show that p_4 depends on q^{max} and ψ . In Figure 12 we plot q^{max} as functions of p_4 for two radiation directions $\psi = 0$ and 70° .

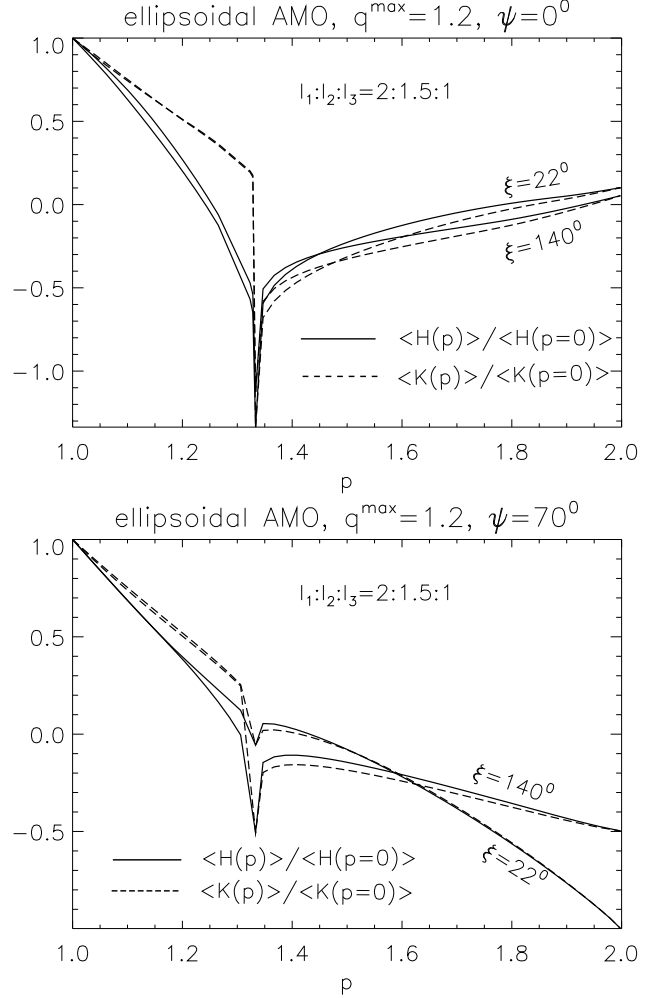


FIG. 6.— Torque components averaged over torque-free motion, $\langle H(p) \rangle$ and $\langle K(p) \rangle$, for different angles ξ and for two radiation directions $\psi = 0^\circ$ and 70° . These torques $\langle H(p) \rangle$ and $\langle K(p) \rangle$ coincide for $p = 1$, I_1/I_2 and I_1/I_3 , corresponding to three stationary points 1, 2 and 3.

In addition, Figure 7 shows that when $p \rightarrow I_1/I_2$, the figure exhibits very sharp changes. In fact, we see the fast changes of $\langle K(J, \xi, p) \rangle_\phi - \langle H(J, \xi, p) \rangle_\phi$ as p increases from slightly smaller than I_1/I_2 to slightly larger than I_1/I_2 . As $p = I_1/I_2$, it becomes zero.

Similar to Figure 7, Figure 8 shows $\langle K(J, \xi, p) \rangle_\phi - \langle H(J, \xi, p) \rangle_\phi$ for the shape 1 (see Fig.4) and AMO with the same ratio of inertia moments $I_1 : I_2 : I_3 = 1.745 : 1.610 : 0.8761$ and $q^{max} = 2.5$, and for $\psi = 0^\circ$. It can be seen that the AMO reproduces well the dependence of RATs on p for the shape 1. For instance, we observe a good correspondence between the stationary points obtained, but the stationary point 4 in the AMO is very close to the point 1 in this case (point 4 is seen in the lower panel of Fig.7).

4.3. Variation of RATs with ξ : stationary points for ξ

Let us consider the forms of RATs as a function of ξ at particular values $p = 1$ (perfect coupling of \mathbf{a}_1 with \mathbf{J}) and I_1/I_3 ($\mathbf{a}_1 \perp \mathbf{J}$) for the same AMO.

In Figure 9 we present the torque components $\langle F(p) \rangle$ and $\langle H(p) \rangle$ for the alignment without high- J attractor, i.e., $q^{max} = 1.2$, $\psi = 0^\circ$ for $p = 1$, I_1/I_2 and I_1/I_3 . We

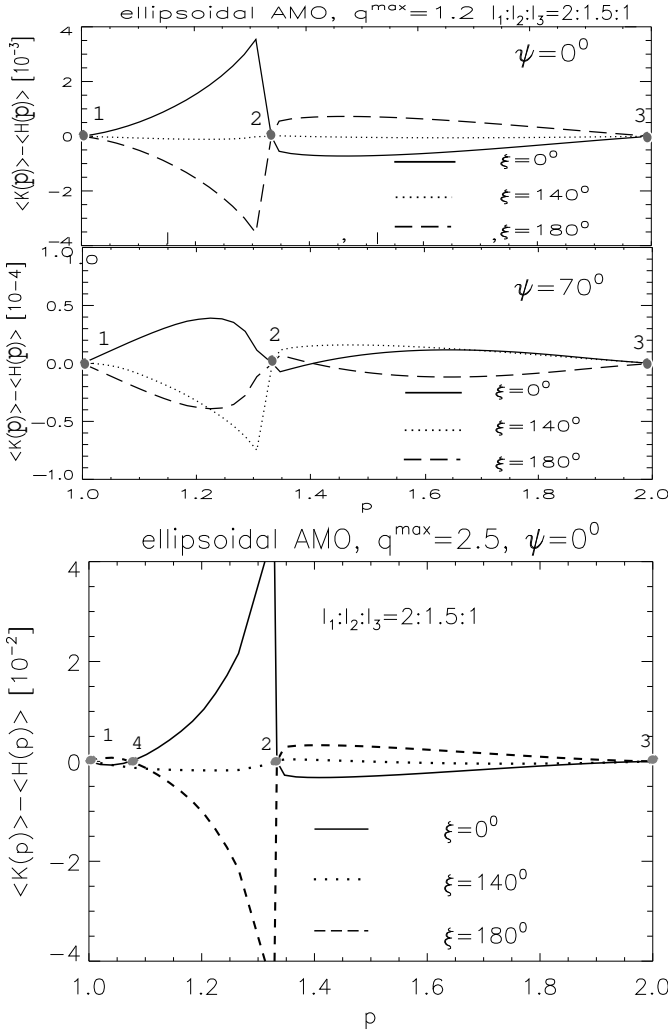


FIG. 7.— Difference between $\langle K(p) \rangle$ and $\langle H(p) \rangle$ for different angles ξ for $\psi = 0^\circ$ and 70° and $q^{\max} = 1.2$ (upper panel) and $\psi = 0^\circ$, $q^{\max} = 2.5$ (lower panel). Zero points denoted by filled circles corresponding to $\langle K \rangle - \langle H \rangle = 0$ are stationary points of p . In the upper panel, three stationary points are 1, 2 and 3, corresponding to $p = 1$, I_1/I_2 and I_1/I_3 . In the lower panel, in addition to stationary points 1, 2 and 3, there exists another stationary point 4.

see that stationary points $\xi = 0$ and π , i.e., points 1 and 6, appear for every p . In addition to these points, for $p = I_1/I_2$ and I_1/I_3 , there exist two other stationary points at $\cos \xi = \pm 9$ (2, 5), and $\cos \xi = \pm 0.35$ (3, 4), respectively. So, in the case of wrong internal alignment, \mathbf{J} may not perfectly aligned with the magnetic field.

The upper panel of Figure 10 is similar to that of Figure 9, but for the case of alignment with high- J attractor with $q^{\max} = 2.5$. For $p = 1$, we see four stationary points (1, 2, 7, 8), where (8) is a high- J attractor. Other stationary points (1, 3, 6, 8) and (1, 4, 5, 8) are for $p = I_1/I_2$ and I_1/I_3 , respectively.

4.4. Helicity versus axis of rotation

For $p = I_1/I_3$, the rotation of the grain is about the axis of minor inertia \mathbf{a}_3 . In this case, RATs depend on the angle between the grain rotation axis \mathbf{a}_3 and the radiation direction \mathbf{k} . This angle is also the angle between \mathbf{J} and \mathbf{B} , ξ , when $\psi = 0^\circ$. Therefore, the dashed line in Figure 9 represents RATs as a function of the angle

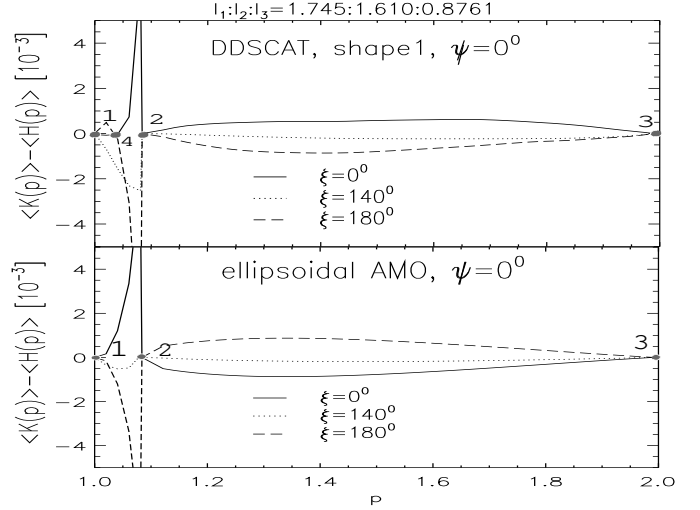


FIG. 8.— Similar to Figure 7 but for shape 1 and AMO with the same ratio of inertia moments $I_1 : I_2 : I_3 = 1.745 : 1.610 : 0.8761$ and $q^{\max} = 2.5$, and for $\psi = 0^\circ$.

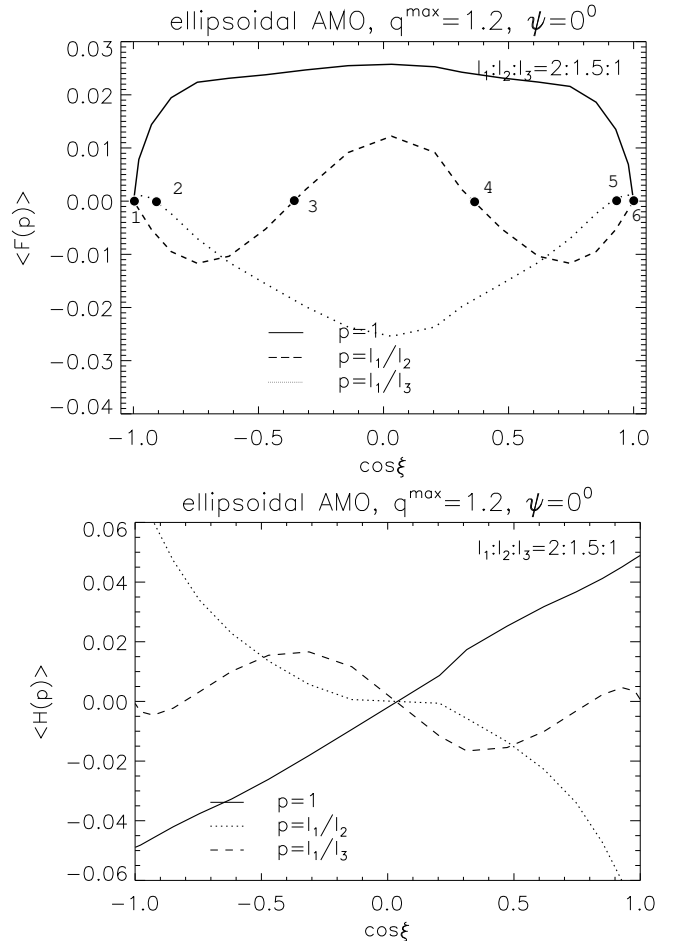


FIG. 9.— Torque components $\langle F \rangle$ and $\langle H \rangle$ for $p = 1$, I_1/I_2 and I_1/I_3 . (1, 6), (1, 2, 5, 6) and (1, 3, 4, 6) are stationary points for $p = 1$, I_1/I_2 and I_1/I_3 , respectively.

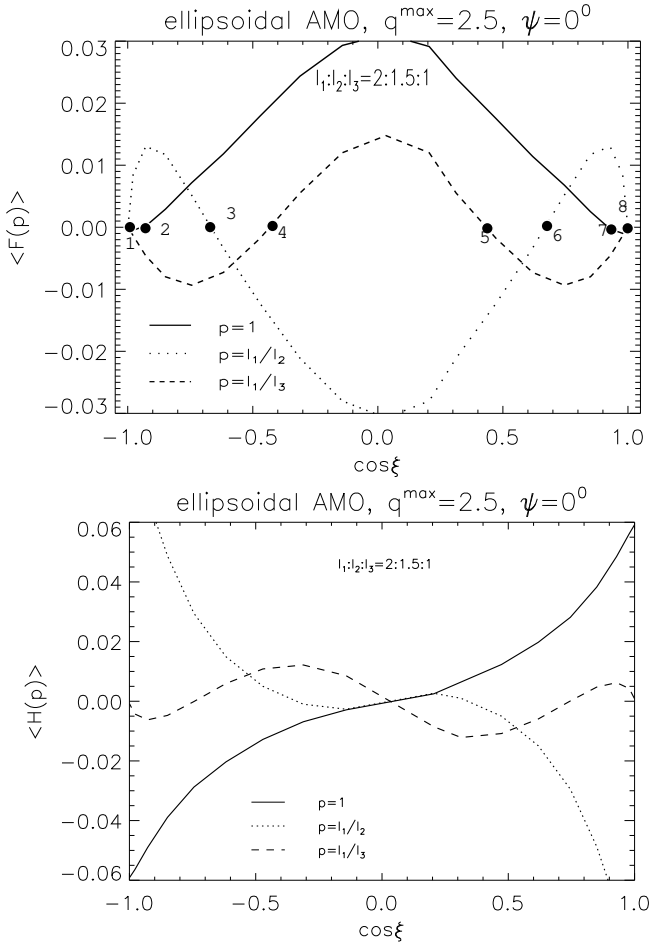


FIG. 10.— Similar to Fig. 9 but for the case $q^{\max} = 2.5$, i.e. alignment with high- J attractor for $\psi = 0^\circ$. (1,2,7,8), (1,3,6,8) and (1,8) are stationary points for $p = 1$, I_1/I_2 and I_1/I_3 , respectively.

between the grain rotation axis and \mathbf{k} .

For $p = 1$, grain rotates about \mathbf{a}_1 described by the angle Θ . Thus, the solid line describes RATs as a function of $\Theta = \xi$. We can see a large difference of $\langle F(p) \rangle$ when the rotation axis changes from the axis of maximum moment of inertia to axis of minor inertia. The lower panel is similar to the upper one, but it shows $\langle H(p) \rangle$. We see that the helicity of the grain for $p = 1$ is similar to that for $p = I_1/I_3$. In other words, the helicity of the grain is identical for the rotation around the maximal and minimal axes.

4.5. Trajectory map

To visualize grain alignment, we present trajectory maps using J, ξ and p , which are the solutions of equations of motion (27)-(31). We adopt initial condition $J_0 = 4I_1\omega_T$, ξ_0 spanning from 0 to π , and $p_0 = 1.1$. Here we consider only one initial value $p_0 < I_1/I_2$ (i.e., grain initially in positive flipping state).

In Figure 11 we present the trajectory maps for the RAT alignment of the triaxial AMO induced by the ISRF for $\psi = 0$ and for $q^{\max} = 1.2$ and 4, corresponding to the alignment without and with high- J attractors (upper and lower panels). In the former case, the alignment occurs at two low- J attractors A and B, where A corresponds to the perfect alignment of \mathbf{J} with \mathbf{B} , and B

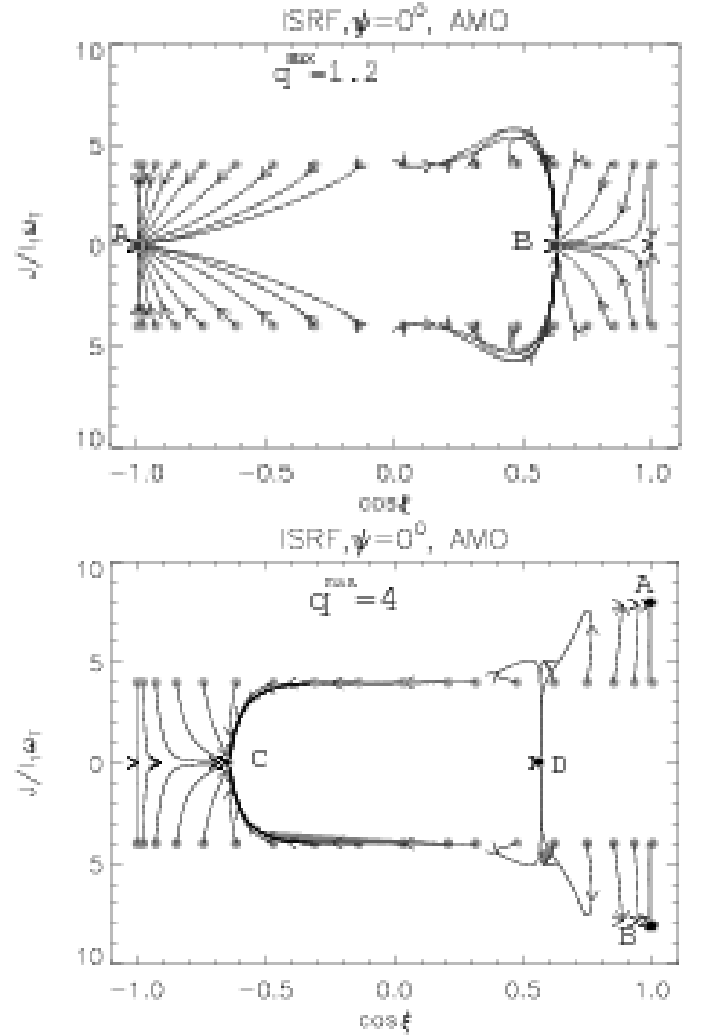


FIG. 11.— Trajectory maps for the RAT alignment of a triaxial ellipsoid using the AMO, in the absence of internal relaxation for the ISRF with direction $\psi = 0^\circ$ and with $q^{\max} = 1.2$ (upper panel) and $q^{\max} = 4$ (lower panel). A and B are low- J attractors in the case $q^{\max} = 1.2$, but there are two high- J attractors A and B for the case $q^{\max} = 4$ (lower panel; here the actual value of J for A and B is 10^2 times the value shown).

corresponds to $\cos \xi = 0.64$. We see that the point B is the new low- J attractor appearing in the absence of internal relaxation.⁸

In the case $q^{\max} = 4$, the alignment has a high- J attractor A at $\cos \xi = 1$, and low- J attractors C and D with $\cos \xi = -0.65$ and 0.65, respectively.

In addition, we studied the radiative alignment for the case $q^{\max} = 0.78$ and $\psi = 70^\circ$, which gives the trajectory map with high- J attractor. We observed that the alignment is similar to the lower panel in Figure 11.

4.6. Internal alignment of grain axes with \mathbf{J}

Let us discuss the internal alignment corresponding to the trajectory maps shown in Figure 11. The initial value of p was assumed to be smaller than I_1/I_2 .

For the alignment without high- J attractor (the upper panel), the point A corresponds to the perfect internal

⁸ LH07a found that for the AMO with $q^{\max} = 1.2$, all grains are driven to one low- J attractor A for $\psi = 0^\circ$

alignment with $p = 1$, while the point B has internal alignment with \mathbf{J} along \mathbf{a}_2 axis, which corresponds to $p = I_1/I_2$.

For the case of alignment with high- J attractor, i.e., $q^{max} = 4$ and $\psi = 0^\circ$ (lower panel of Fig. 11), the internal alignment depends on the initial value of p_0 . If $p_0 < p_4$, then the lower panel of Figure 7 shows that $\langle K(p) \rangle - \langle H(p) \rangle < 0$ for $\cos \xi_0 \sim 1$. As a result, after some time, p decreases to $p = 1$, i.e., perfect internal alignment, and the aligning torque $\langle F(p) \rangle$ approaches $\langle F(p = 1) \rangle$. Therefore, the alignment returns to the case of perfect coupling of \mathbf{a}_1 with \mathbf{J} as studied in DW97 and LH07a, i.e., the alignment of \mathbf{J} with \mathbf{B} is determined by $\langle F(p = 1) \rangle$ and $\langle H(p = 1) \rangle$. LH07a found that for the AMO with $q^{max} > 2$ and $\psi = 0^\circ$, the alignment has high- J attractors. We can see it in the lower panel of Figure 11 for $q^{max} = 4$. Combined with the internal alignment, the high- J attractor corresponds to $\mathbf{J} \parallel \mathbf{B}$ and long grain axes perpendicular to \mathbf{B} . For $\cos \xi_0 \sim -1$, we have $\langle K(p) \rangle - \langle H(p) \rangle > 0$, so p increases from p_0 to p_4 if $p_0 < p_4$. Thus, the low- J attractor corresponds to the alignment with $p = p_4$. As a result, A and B correspond to the internal alignment with $\mathbf{a}_1 \parallel \mathbf{J}$, and C corresponds to internal alignment with $\mathbf{a}_1 \perp \mathbf{J}$. If $p_0 > p_2$, then there are two attractors with $p = p_4$ and p_2 .

Since the stationary point p_4 is important in determining the type of alignment, in the upper panel of Figure 12 we plot q^{max} against p_4 , for two light beam directions $\psi = 0^\circ$ and 70° . Shaded areas describe the alignment with high- J attractor corresponding to a perfect alignment of \mathbf{J} with \mathbf{B} and perfect internal alignment, i.e., $\mathbf{a}_1 \parallel \mathbf{J}$.

The lower panel of Figure 12 presents the alignment depending on q^{max} and ψ .

Moreover, when the internal alignment happens with $p = 1$, then, we can predict the alignment for different ψ if we know q^{max} . The result is presented in the lower panel of Figure 12. The solid curves, characterizing the boundary for the alignment with high- J attractor, are obtained assuming that $p_0 < p_4$. We see that the alignment here is similar to what found in LH07a. We note that at $p = 1$, the average over the wobbling for irregular grains is identical with the averaging over the rotation angle β used in LH07a.

We note that the internal alignment with $p = I_1/I_2$ corresponds to the rotation of a grain along the axis of intermediate inertia moment \mathbf{a}_2 . For torque-free motion, this rotation is unstable. Therefore, gas bombardment can destabilize this internal alignment, and grains may return to the alignment with short or long axes perpendicular to \mathbf{J} .

4.7. RAT alignment in presence of weak internal relaxation

Let us consider a regime of weak internal relaxation, i.e., when $t_{rad} < t_{int} < t_{gas}$. Figure 5 shows that grains with size in the range 1.5 to 6 μm correspond to this situation. For this regime, it is convenient to introduce a new radiative timescale, t'_{rad} , which is defined by (using eq. 31)

$$t'_{rad} = \frac{I_1 \omega}{M |\langle K(p) \rangle - \langle H(p) \rangle|_{max}}, \quad (32)$$

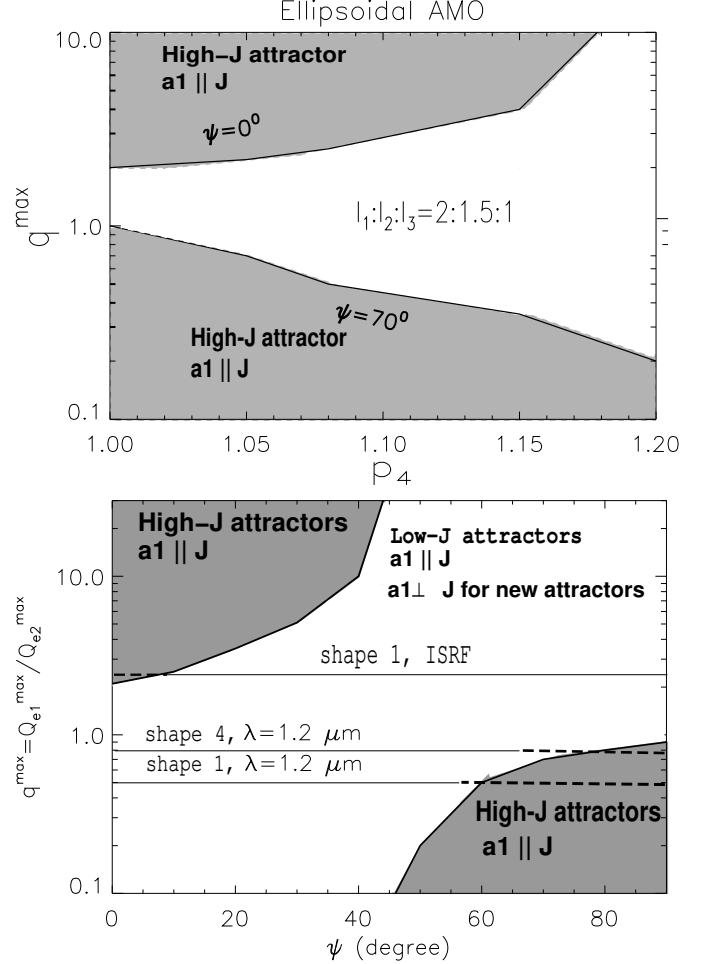


FIG. 12.— *Upper*: Diagram showing the dependence of p_4 —the value of p at the stationary point 4 (see Fig. 7 and 8) as function of q^{max} for two light directions $\psi = 0$ and 70° . Shaded areas represent the internal alignment when the initial value, p_0 smaller than p_4 . *Lower panel*: Diagram showing the alignment type depending on q^{max} and ψ when $p_0 < p_4$.

where max denotes the maximal value of $|\langle K(p) \rangle - \langle H(p) \rangle|$ as a function of p for given angles ξ and ψ .

It can be seen that t'_{rad} is about one order of magnitude larger than t_{rad} given by equation (20). Therefore, it is possible to have $t'_{rad} > t_{int} > t_{rad}$. For this case, one interesting effect occurs with the wrong alignment previously discussed is that grains are driven to right alignment on a characteristic time t_{int} . However, for practical purposes, a change from t_{rad} to t'_{rad} is marginal due to a steep dependence.

5. RAT ALIGNMENT BY DIPOLE AND QUADRUPOLE COMPONENTS OF RADIATION FIELD

All earlier studies of the RAT alignment (DW96, DW97, WD03; LH07, LH08, HL08ab) have been done assuming that the radiation field can be described by a unidirectional beam directed along \mathbf{k} (see Fig. 1) with a degree of anisotropy γ . This assumption is consistent with grains near a point radiation source. In many circumstances, e.g., in molecular clouds, and even in some diffuse clouds, the approximation of radiation field by dipole and quadrupole is more appropriate.

Below, we study the RAT alignment induced by the dipole and quadrupole fields. For the sake of simplicity,

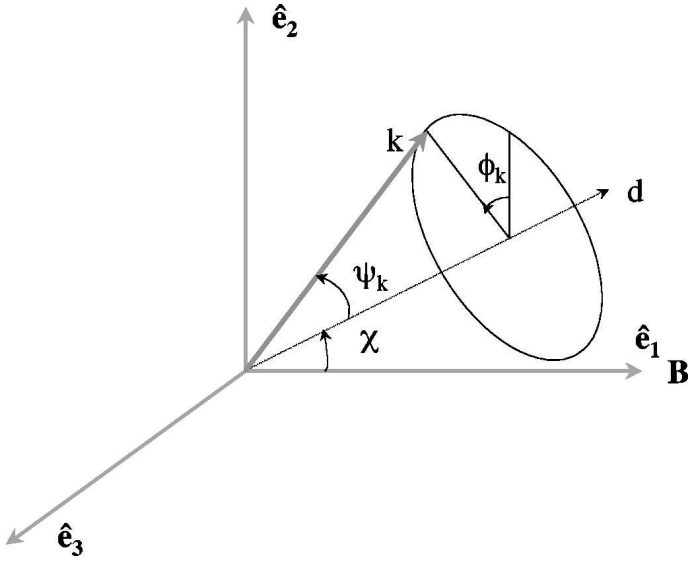


FIG. 13.— The lab coordinate system $\mathbf{e}_1\mathbf{e}_2\mathbf{e}_3$ for the dipole field: \mathbf{B} is the magnetic field direction, \mathbf{d} is the dipole axis, χ is the angle between the dipole axis \mathbf{d} and the magnetic field \mathbf{B} , \mathbf{k} is the radiation direction. ϕ_k, ψ_k describe the direction of radiation \mathbf{k} in the lab coordinate system. we assume that the axis of maximum moment of inertia \mathbf{a}_1 is constrained to be parallel to angular momentum \mathbf{J} (i.e., thermal fluctuations and thermal flipping are completely disregarded; see DW97; LH07a). In fact, our study in HL08a proved that this is a sufficiently good approximation unless we want to calculate the exact degree of alignment.

5.1. Coordinate systems

We define a lab coordinate system $\mathbf{e}_1\mathbf{e}_2\mathbf{e}_3$ (\mathbf{e}_i -system), with \mathbf{e}_1 parallel to \mathbf{B} , $\mathbf{e}_2 \perp \mathbf{e}_1$, lies in a plane formed by the magnetic field \mathbf{B} and the dipole axis \mathbf{d} for dipole field or symmetric axis for the quadrupole field, and \mathbf{e}_3 perpendicular to the plane \mathbf{e}_1 and \mathbf{e}_2 (see Fig. 13).⁹ Let χ be the angle between \mathbf{d} and \mathbf{B} , and define a coordinate system $\mathbf{e}_1^x\|\mathbf{d}, \mathbf{e}_2^x\|\mathbf{e}_3^x$ with $\mathbf{e}_3^x = \mathbf{e}_3$, so-called \mathbf{d} -system. Now, the radiation direction \mathbf{k} in the \mathbf{d} -system is determined by two angles ψ_k and ϕ_k (see Fig. 13). Since RATs depend on the angle between grain axes \mathbf{a}_i and the radiation direction \mathbf{k} , let us define a coordinate system \mathbf{e}_1^0 with $\mathbf{e}_1^0\|\mathbf{k}$, \mathbf{e}_2^0 lying in the plane \mathbf{k} and \mathbf{d} , and \mathbf{e}_3^0 perpendicular to this plane. The orientation of a grain in the \mathbf{e}_i^0 system is described by three angles Θ, β and Φ (see the upper panel of Fig. 1 with \mathbf{e}_i are replaced by \mathbf{e}_i^0). The transformation between these coordinate systems are described in Appendix D.

5.2. Dipole Component

For a given direction of the grain in the lab coordinate system, the net RAT resulting from a dipole radiation field is given by

$$\Gamma_{rad} = \sum_{k=1}^N \mathbf{Q}(\psi_k)_\Gamma \frac{\gamma \bar{\lambda} a^2 u_d(\psi_k)}{2} \frac{\Delta\Omega_k}{2\pi}, \quad (33)$$

where ψ_k is the angle between the radiation direction \mathbf{k} and the dipole axis \mathbf{d} , γ is the degree of anisotropy,

⁹ The symmetric axis of the quadrupole field is defined by two dipole axes.

$u_d(\psi_k)$ is the energy density of dipole field, $\Delta\Omega_k = \pi/N$ is the element of solid angle in the direction ψ_k , and the summation (33) is performed in the range ψ_k from $-\pi/2$ to $\pi/2$ (i.e., only outward radiation is accounted for). The spatial distribution of dipole radiation intensity is given by the usual expression

$$u_d(\psi_k) = u_{ISRF} \sin^2 \psi_k. \quad (34)$$

We assume in equation (34) that the energy density of the dipole field has the same amplitude to that of the ISRF, and we deal only with its spatial distribution.

To study the RAT alignment, we need to know components of torques in the lab coordinate system, i.e., $Q_{e_1}(\xi, \psi, \phi), Q_{e_2}(\xi, \psi, \phi)$ and $Q_{e_3}(\xi, \psi, \phi)$. It is straightforward, but tedious to obtain $Q_{e_i}(\xi, \psi, \phi)$ from $Q_\Gamma(\Theta, \beta, \Phi)$ given by equations (A4)-(A5) through a series of coordinate transformation. Firstly, we perform the transformation from \mathbf{k} -system to \mathbf{d} -system, then, from \mathbf{d} -system to \mathbf{e}_i -system. Finally, we average the resulting torques in the spherical system J, ξ, ϕ over the azimuthal angles of \mathbf{k} about dipole axis, ϕ_k , and the Larmor precession angle ϕ (see Appendix E for more detail).

Using the obtained RATs, we solve the equations of motion to find J, ξ as functions of time, and present their evolution in terms of phase trajectory maps (see LH07a for more detail). As an example, we use the AMO for a grain size $a = 0.2\mu\text{m}$, and $q^{max} = 3.5$. For the dipole radiation field with $\chi = 0^\circ$, the torque components and the corresponding trajectory map are shown in the upper and lower panel of Figure 14, respectively. The upper panel shows the existence of stationary points at $\cos\xi \sim \pm 1$. It is possible to check that the stationary point $\cos\xi = 1$ is an attractor because $\langle F' \rangle_\phi / \langle H \rangle_\phi |_{\cos\xi=1} < 0$ and $\langle H \rangle_\phi > 0$. This high- J attractor is denoted by a circle (A) in the trajectory map (see lower panel). In addition, there exists also a low- J attractor B, as usual. Both stationary points correspond to a perfect alignment of angular momentum with the magnetic field.

5.3. Quadrupole Component

Let us consider now the RAT alignment by the quadrupole component of radiation field. The spatial distribution of the energy density for the quadrupole field is given by

$$u_{quad} = u_{ISRF} \sin^2 \psi_k \cos^2 \psi_k, \quad (35)$$

where ψ_k is the angle between radiation direction and the symmetric axis of the quadrupole. Following the same procedure as with the dipole field, we obtain results for the AMO with $q^{max} = 0.78$ (i.e., similar to the value of the shape 2 at $\lambda = 1.2\mu\text{m}$, see LH07a) and the grain size $a_{eff} = 0.2\mu\text{m}$ in Figure 15 for two directions of the quadrupole with the magnetic field: $\chi = 0^\circ$ (upper panel) and 45° (lower panel). The alignment occurs without high- J attractors in the former case, but with a high- J attractor in the later one.

5.4. Simultaneous action of dipole and quadrupole components

Figure 16 shows the existence of high- J and low- J attractors as functions of q^{max} and χ for the dipole (upper panel) and quadrupole (lower panel) fields. For the

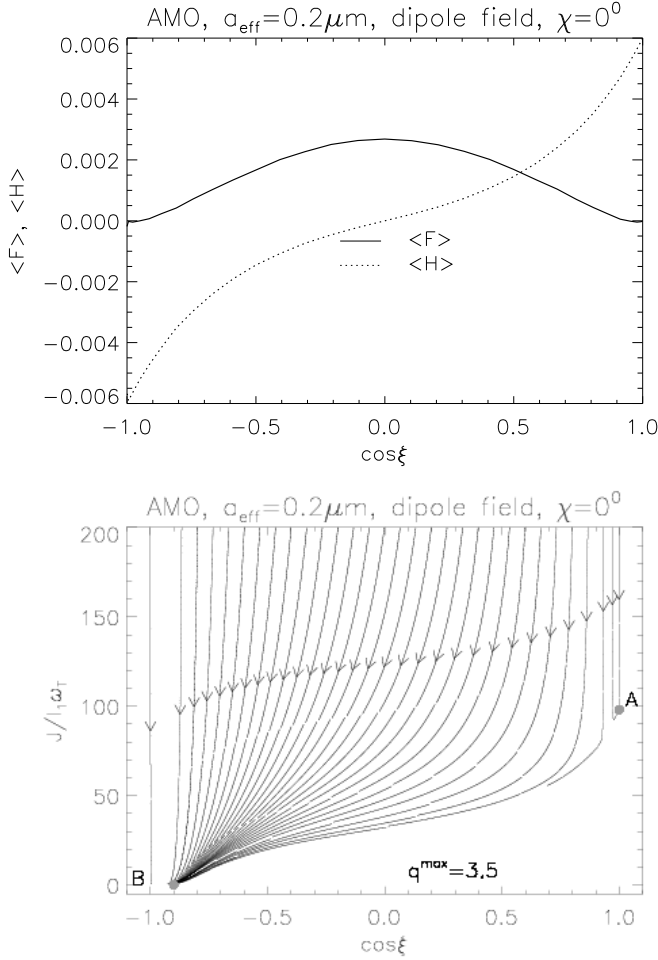


FIG. 14.— *Upper panel:* Aligning, $\langle F \rangle_\phi$, and spin-up, $\langle H \rangle_\phi$ components for the AMO with $q^{max} = 3.5$ induced by the dipole radiation field with $\chi = 0$. *Lower panel:* The phase trajectory map obtained by torques in the upper panel. A is a high- J attractor corresponding to the perfect alignment of \mathbf{J} with respect to \mathbf{B} , and B is a low- J attractor.

dipole field, it can be seen that the high- J attractor appears when $q^{max} > 3.2$ for $\chi = 0^\circ$, then increases with χ increasing, and $q^{max} > 100$ for $\chi = 30^\circ$. For $\chi > 30^\circ$, the high- J attractor exists when $q^{max} < 1.8$. On the other hand, for the quadrupole field, there is the high- J attractor when $q^{max} < 2.5$ for a wide range $\chi > 20^\circ$.

LH07a have calculated RATs for a number of irregular grain shapes, grain size and wavelength, and found that for the majority of shapes we have $q^{max} < 10$. Thereby, from Figure 16 we see that the possibility of alignment with high- J attractor is enhanced for both the dipole and quadrupole fields compared to a single beam.

In the upper panel of Figure 17, we present the ratio of energy density of dipole to quadrupole components, u_d/u_q , as a function of χ for the AMO with $q^{max} = 1.2$. For this AMO, the high- J attractor appears frequently (see Fig. 16upper). It reveals that the energy density of dipole component is required to be dominant over that of quadrupole in order to have high- J attractor for $\chi < 20^\circ$. In the range $\chi > 30^\circ$, the high- J attractor does not depend on the ratio of their energy density, because both components produce high- J attractors.

Apart from the existence of high- J attractors, the value

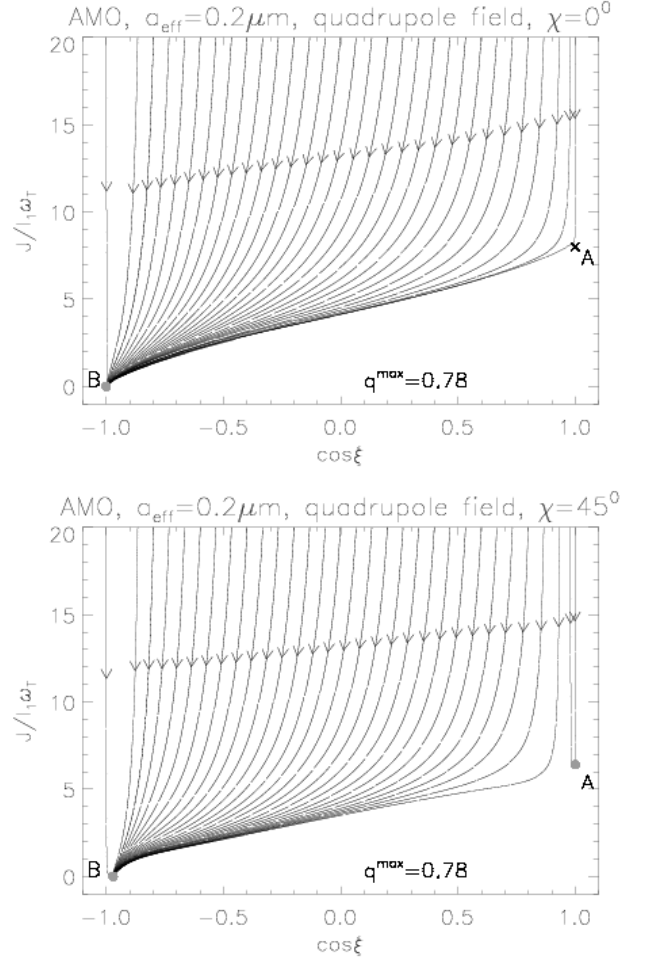


FIG. 15.— RAT alignment by the quadrupole field with $q^{max} = 0.78$ for $\chi = 0^\circ$ (upper panel) and 45° (lower panel), respectively. In the upper panel, A is a high- J repeller, and B is a low- J attractor, both corresponding to the perfect alignment of \mathbf{J} with respect to \mathbf{B} . In the lower panel, A becomes a high- J attractor and B is a low- J attractor.

of angular momentum J at these points is essential for calculations of degree of alignment. It is easy to see that the angular momentum achievable (i.e., maximal value) depends on the angle χ .

Now, let us adopt the irregular grain (shape 1) with RATs obtained using DDSCAT, and calculate the value of the maximal angular momentum $J_{max}(\chi) = I_1 \omega_{max}(\chi)$ produced by dipole and quadrupole components of the ISRF as a function of the angle χ . The anisotropy degree of radiation $\gamma = 0.1$ is assumed for all components. We compare the results with that induced by a beam of radiation.

In the lower panel of Figure 17 we present the resulting value of $\omega_{max}(\chi)$. There it can be seen that $\omega_{max}(\chi)$ decreases rapidly with increasing χ for the dipole component, but it exhibits slow change for the quadrupole component. In addition, ω_{max} induced by the dipole component is ~ 10 times greater than that by the quadrupole one. Therefore, when we only focus on the effect of spin-up by RATs, the quadrupole component can be neglected. The dipole component results in lower values of ω_{max} compared to that produced by the radiation beam (see Fig. 17, lower), as a result of the average over the

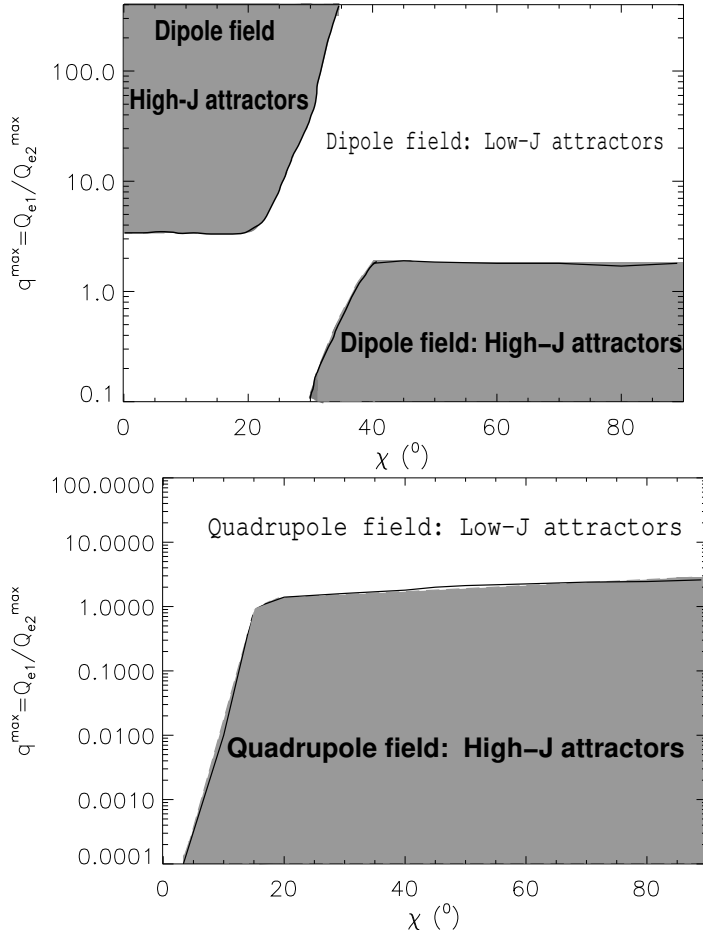


FIG. 16.— Diagram depicting the existence of high- J and low- J attractors depending on q^{\max} and χ for dipole field (*Upper panel*) and quadrupole field (*Lower panel*). The shaded area represents the domain of the co-existence of high- J attractors and low- J attractors, and the white area represents the presence of low- J attractors only.

entire space for the dipole field.

5.5. Implications for grain alignment

The degree of RAT alignment depends strongly on the possibility of existence of high- J attractors (see HL08a). In LH07a, we identified the criteria for the existence of high- J as a function of the angle between the beam direction and the magnetic field. There it is shown that the high- J attractor occurs when $q^{\max} > 2$ for $\psi < 45^\circ$, and $q^{\max} < 1$ for $\psi > 45^\circ$. In other words, there is a gap of q^{\max} from 1 to 2, in which there is no high- J attractors, irrespective of grain shape and size. Fortunately, the dipole and quadrupole radiation can produce the high- J attractors for $q^{\max} < 2$ (see Fig. 17) for $\chi > 30^\circ$. It indicates that the dipole and quadrupole extends the range of high- J attractor and enable us to have high- J attractors for $q^{\max} = 1$ to 2. This range is easily satisfied for irregular grains (see LH07a) in a wide range of λ/a_{eff} . Therefore, an enhancement of the degree of the RAT alignment is expected for the dipole and quadrupole field compared to the case of a radiation beam.

6. DISCUSSION

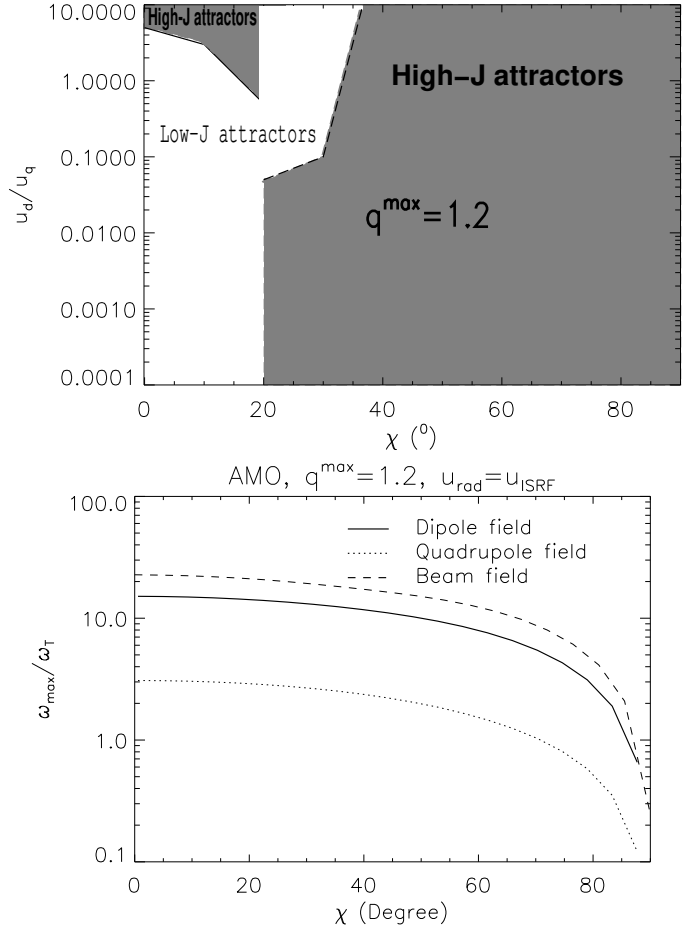


FIG. 17.— *Upper panel*: Ratio of energy density of dipole to quadrupole components, u_d/u_q , for which grains are aligned with high- J attractors for the AMO with $q^{\max} = 1.2$. The shaded area represents the domain of the co-existence of high- J attractors and low- J attractors, and the white area represents the presence of low- J attractors only. *Lower panel*: The maximal value of angular velocity for a grain size $0.2\mu\text{m}$, as a function of χ for dipole and quadrupole fields and one beam field. For the later, χ denotes ψ the angle between the beam direction and the magnetic field.

In the rest of this section we provide a brief account of our accomplishments in the paper and present our outlook on the further work in the field of grain alignment.

6.1. Alignment in environments different from ISM: large grains

Traditionally, grain alignment was the topic of interstellar medium (ISM) research. The gap between the studies of polarized radiation from aligned dust in environments other than the ISM and the theory of grain alignment got so wide that the researchers outside the ISM domain sometimes write papers about aligned dust and do not refer to *any* theoretical work on grain alignment. However, there is ample evidence of grain alignment in non-ISM environments (see Tamura et al. 1999; Rosenbush et al. 2007; Hough et al. 2007).

In many of these environments, e.g., for dust in comets and circumstellar dust, the radiation field is stronger than in the ISM, thus RATs are stronger. One difference that one faces there is that grains may be substantially larger. As we demonstrated in the paper, for larger grains the internal relaxation gets slower, which makes one won-

der whether the RAT alignment happens very differently from the ISM case. Our study shows that the direction of alignment of the angular momentum \mathbf{J} with respect to the magnetic field \mathbf{B} is similar to that in the presence of strong internal relaxation. This alignment can be perfect with high- J and/or low- J attractors, depending on the factor q^{max} . However, the alignment of grain axes with respect to \mathbf{J} depends on the initial angle between them, more precisely, on the initial value of dimensionless parameter p . If this angle is smaller than a particular value, p_4 , defined in the main text, which is a function of q^{max} , the grain axis of maximum moment of inertia \mathbf{a}_1 gets aligned along \mathbf{J} , and both \mathbf{a}_1 and \mathbf{J} become aligned with \mathbf{B} . HL08b showed that pinwheel torques (e.g., H_2 formation, isotropic radiative torque, etc.) increase fast with the grain size. As a result, large grains can be spun up to suprathermal rotation with $J \gg J_{th}$. The direct effect of suprathermal rotation is the alignment of \mathbf{a}_1 and \mathbf{J} .

Table 1 compares our results for grains without and with internal relaxation using the AMO. We can see that for high- J attractors, the alignment is the same in both cases. We note that the results in the later case were shown to be consistent with the alignment of irregular grains obtained by DDSCAT. However the general case of alignment of large irregular grains in the absence of internal relaxation requires further studies to confirm the predictions obtained with the AMO. Further studies should consider also the effect of pinwheel torques on the alignment in the absence of internal relaxation.

6.2. Utility of AMO

The analytical model (AMO) was introduced in LH07a to describe the case of alignment in the presence of *perfect* alignment of \mathbf{J} with the axis of maximal moment of grain inertia. It provided excellent representation of the alignment of irregular grains within this approximation. Later in HL08a and HL08b we applied AMO to grains in the presence of thermal fluctuations, which at small values of J partially randomize the alignment of \mathbf{J} with the aforementioned axis. Nevertheless, AMO happened to do a nice job in these cases, adequately describing the behavior of irregular grains.

The case of no internal alignment is the extreme case of testing AMO. For instance, AMO has only one helicity axis, while multiple helicity axes are possible for an irregular grain. It is interesting, that even for this case, our limited testing is indicative of the AMO's utility.

6.3. Towards modeling of polarized radiation

Similar to the polarimetric work of non-ISM observers, the modeling of polarization arising from aligned grains has been mostly developing without much connection to the theory of grain alignment. Exceptions from this rule include Cho & Lazarian (2005, 2007), Pelkonen et al. (2007), Bethell et al. (2007), and Falceta-Golcaves et al. (2008). However, this modeling was done on the basis of somewhat ad hoc alignment prescriptions, which should be improved as the theory gets predictive.

A step towards a more reliable polarization modeling is done in this paper where we considered grain alignment induced by the dipole and quadrupole components¹⁰ of

the radiation field. The earlier studies assumed that the radiation was coming from a particular direction, which is, for instance, not the case for most of the grains in starless cores or accretion disks. In the latter cases it is proper to decompose the radiation field in multipoles and consider the effects of the individual components. Our study shows that the parameter space for having high- J attractors differs for the alignment by the different multipole components.

Moreover we identified the range of torque ratio, q^{max} , for which the presence of dipole and quadrupole components of radiation field results in the alignment with high- J attractors. The required range q^{max} is fulfilled for irregular grains studied in HL08a.

6.4. Credit to Dolginov & Mytrophanov 1976

In our paper we showed that the analytical results on RATs in Dolginov & Mytrophanov (1976) were incorrect (see Fig. 18). Therefore, naturally, our present results on the RAT alignment obtained for grains in the absence of internal relaxation, which was also the assumption in Dolginov & Mytrophanov (1976) study, differ from those in the study. This should not, however, undermine the pivotal significance of the the Dolginov & Mytrophanov paper¹¹. This paper is important as it *discovered* RATs and discussed the possibility of irregular grains being aligned by RATs, even if it failed to describe it quantitatively. In addition, the notion of grain helicity, which is the central concept of AMO, can be traced back to Dolginov & Mytrophanov (1976) work. Moreover, as we mentioned in the introduction, the problem was so hard that the papers that followed Dolginov & Mytrophanov (1976), in all its complexity, were not able to capture correctly the physics of the RAT alignment either.

6.5. Other processes

Our paper, for the sake of simplicity, does not consider the effect of the pinwheel torques. Such torques, e.g. torques arising due to H_2 formation over catalytic sites over grain surface (Purcell 1979), were discussed in the framework of the RAT alignment in Hoang & Lazarian (2008b) for grains with strong internal relaxation. A study of effect of these torques on large grains, for which the effects of internal relaxation are reduced, will be done elsewhere. In addition, in our paper we considered the RAT alignment in respect to magnetic field. As we discussed in LH07a, for a sufficiently slow rate of Larmor rotation, the alignment can happen also in respect to the radiation field. If, however, grains have superparamagnetic inclusions the rate of rotation increases substantially. This, potentially, provides another way of testing whether grains have or do not have superparamagnetic inclusions.

7. SUMMARY

tipoles of the radiation field is to study the alignment numerically at every point of the data cube using the radiation field at the particular point. Naturally, this would entail much more intensive computations.

¹¹ Incidentally, the same paper discusses for the first time the Barnett effect in the application to interstellar grains. This induced the all-important notion of fast Larmor precession of grains and helped E. Purcell to discover the effect of Barnett relaxation.

¹⁰ The alternative to modeling the RAT alignment by the mul-

In this paper we continued our work on the RAT alignment using both AMO and DDSCAT calculations of torques. Our principal results in the paper above can be summarized as follows:

- We identified the range of grain size for which the internal relaxation within a normal paramagnetic grain is not important.

- We demonstrated that, in the absence of internal relaxation, RATs can align the grain's angular momentum with respect to the magnetic field, which is similar to the alignment in the presence of strong internal relaxation. For the internal alignment of grain axes with the angular momentum, it can be perfect, i.e. $\mathbf{a}_1 \parallel \mathbf{J}$ when the initial angle between them is small.

- We studied the RAT alignment induced by dipole and quadrupole components of the radiation field assuming perfect internal alignment of grain axis of maximum moment of inertia with the angular momentum due to *strong internal relaxation*. Using the AMO, we found that the

parameter space for the existence of high-J attractors is extended compared to the earlier studied case of a single direction radiation. This parameter space is given by the range of q^{max} and the angle χ between the symmetric axis of dipole and quadrupole radiation fields and the magnetic field. Therefore, higher degrees of radiative alignment are expected.

- Our study for the joint action of dipole and quadrupole components showed that for the angle χ between the dipole and quadrupole axis and the radiation direction smaller than ~ 20 degree, the dipole component has to be dominant over quadrupole one in order to align grains with high-J attractors.

ACKNOWLEDGMENTS

We acknowledge the support by the NSF Center for Magnetic Self-Organization in Laboratory and Astrophysical Plasmas and NSF grant AST 0507164.

REFERENCES

- Andersson, B-G, Potter, S.B. 2007, ApJ, 665, 369
 Bethell, T., Cherpunov, A., Lazarian, A., Kim, J. 2007, ApJ, 663, 1055
 Bradley, J.P., 1994, Science, 265(5174), 925-929
 Cho, J., Lazarian A. 2005, ApJ, 631, 361
 Cho, J., & Lazarian, A. 2007, ApJ, 669, 1085
 Crutcher, R.M., Nutter, D.J., Ward-Thompson, D., & Kirk, J.M. 2004, ApJ, 600, 279
 Davis, L., Greenstein J.L. 1951, ApJ, 114, 206
 Dolginov, A.Z. 1972, Ap&SS, 16, 337
 Dolginov, A.Z., Mytrophanov, I.G. 1976, Ap&SS, 43, 291
 Dolginov, A.Z., Silantev, N.A. 1976, Ap&SS, 43, 337
 Falceta-Golcaves, D., Lazarian, A., & Kowal, G. 2008, ApJ, in press
 Gold, T. 1952, Nature, 169, 322
 Goodman, A.A., Jones, T.J., Lada, E.A.; Myers, P.C. 1995, ApJ, 448
 Goodman, A.A., & Whittet, D.C.B. 1995, ApJ, 455
 Draine, B., Flatau, P. 1994, J. Opt. Soc. Am. A., 11, 1491
 Draine, B., Lazarian, A. 1998, ApJ, 508, 157
 Draine, B., Weingartner, J. 1996, ApJ, 470, 551 (DW96)
 Draine, B. Weingartner, J. 1997, ApJ, 480, 633 (DW97)
 Hall, J. 1949, Science, 109, 166
 Harwit, M. 1970, Nature, 226, 61
 Hildebrand et al. 2000, PASP, 112
 Hildebrand, R. 2002, in *Astrophysical Spectropolarimetry*, ed. by J. Trujillo-Bueno, F. Moreno-Insertis, & F. Sanchez (Cambridge, UK: Cambridge Univ. Press), p. 265
 Hiltner, W. 1949, Science, 109, 165
 Hoang, T. & Lazarian, A. 2008a, MNRAS (HL08a)
 Hoang, T. & Lazarian, A. 2008b, ApJ, submitted (HL08b)
 Hough, J.H., Lucas, P.W., Bailey, J.A., Tamura, M. 2007, ASPC, 364, 523
 Jones, R.V., & Spitzer, L., Jr, 1967, ApJ, 147, 943-964
 Lazarian, A. 1994, MNRAS, 268, 713
 Lazarian, A. 1995, ApJ, 453, 229
 Lazarian, A. 1997a, MNRAS, 288, 609
 Lazarian, A. 1997b, ApJ, 483, 296
 Lazarian, A. 2007, J. Quant. Spectrosc. Rad. Trans., 106, 225
 Lazarian, A. 2008, arXiv:0811.1020
 Lazarian, A., Draine, B. 1999a, ApJ, 516, L37 (LD99a)
 Lazarian, A., Draine, B. 1999b, ApJ, 520, L67 (LD99b)
 Lazarian A., Efroimsky M. 1999, MNRAS, 303, 673
 Lazarian, A., Goodman, A.A., Myers P.C. 1997, ApJ, 490, 273
 Lazarian, A., Roberge, W. 1997, ApJ, 484, 230
 Lazarian, A., Hoang, T. 2007a, MNRAS, 311, 903 (LH07a)
 Lazarian, A., Hoang, T. 2007b, ApJL, 669, L77
 Lazarian, A., Hoang, T. 2008, ApJL, 676, L25 (LH08)
 Lazarian A., Yan H. 2002, ApJ, 566, L105-L108
 Lee H., Draine B. 1985, ApJ, 290, 211
 Mathis, J.S. 1986, ApJ, 308, 281-287
 Mathis, J. S., Rumpl, W., & Nordsieck, K. H. 1977, ApJ, 217, 425 (MRN)
 Mathis, J., Mezger, P., Panagia, N. 1983, A&A, 128, 212
 Morish, A.H. 1980, The Physical Principles of Magnetism, New York: W.A. Benjamin
 Pelkonen, V. M, Juvela, M., Padoan, P. 2007, A&A, 461, 551
 Cameron, A.G.W., New York: Neal Watson, 155
 Purcell, E. 1979, ApJ, 231, 404
 Purcell, E., Spitzer, L. 1971, ApJ, 167, 31
 Tamura, M., Hough, J.H., Greaves, J.S., Morino, J-I, Chrysostomou, A., Holland, W.S., & Momose, M. 1999, ApJ, 525, 832-836
 Roberge, W., Hanany, S. 1990, B.A.A.S., 22, 862
 Roberge, W., DeGraf, T.A., Flatherty, J.E. 1993, ApJ, 418, 287 (RDG93)
 Roberge, W., Hanany, S., Messinger, D. 1995, 453, 238
 Roberge, W.G., & Lazarian, A. 1999, MNRAS, 305, 615
 Rosenbush, V., Kolokolova, L., Lazarian, A., Shakhovskoy, N., Kiselev, N. 2007, Icarus, 186, 317
 Spitzer, L., McGlynn, T. 1979, ApJ, 231, 417
 Spitzer, L, Tukey, John W. 1951, ApJ, 114, 187
 Weingartner J., & Draine B. 2003, ApJ, 589, 289
 Weingartner J., & Draine B. 2001, ApJ, 548, 296 (WD01)
 Whittet, D.C.B., Gerakines, P.A., Hough, J.H. & Sneyoy 2001, ApJ, 547
 Whittet D.C.B, Hough J.H, Lazarian A., Hoang T. 2008, ApJ, 674, 304
 Yan H., & Lazarian A. 2003, ApJ, 592, L33-36
 Yan H., Lazarian A., Draine B. 2004, ApJ, 616, 895

APPENDIX

TABLE 1
COMPARISON OF RADIATIVE ALIGNMENT FOR AMO

<i>Without internal relaxation (this work)</i>		<i>With internal relaxation (LH07a)</i>	
High-J attractors	Low-J attractors	High-J attractors	Low-J attractors
$\mathbf{J} \parallel \mathbf{B}$	\mathbf{J} aligned parallel or at some angle with \mathbf{B}	$\mathbf{J} \parallel \mathbf{B}$	\mathbf{J} aligned parallel or at some angle with \mathbf{B}
Long axes $\perp \mathbf{B}$	Long axes \perp or $\parallel \mathbf{J}$	Long axes $\perp \mathbf{B}$	Long axes $\perp \mathbf{B}$

RATS FOR THE ANALYTICAL MODEL: AMO

RAT for the toy model in Figure 2 is given by

$$\mathbf{\Gamma}_{rad} = \frac{\gamma u_{rad} \lambda l_2^2}{2} \mathbf{Q}_{\Gamma}, \quad (\text{A1})$$

where $\mathbf{Q}_{\Gamma} = (Q_{e_1} \mathbf{e}_1 + Q_{e_2} \mathbf{e}_2 + Q_{e_3} \mathbf{e}_3)$ is the vector of RAT efficiency, with Q_{e_1}, Q_{e_2} and Q_{e_3} the components of \mathbf{Q}_{Γ} in the laboratory system. Here l_2 is the size of the squared mirror, λ is the wavelength, and u_{rad} is the energy density in unit erg cm^{-3} of the radiation field.

Using the self-similar scaling of the magnitude of RATs obtained for an irregular grain of size a illuminated by radiation field of wavelength λ ,

$$|Q_{\Gamma}| \sim 0.4 \left(\frac{\lambda}{a}\right)^{-3} \quad \text{for } \lambda > 1.8a, \quad (\text{A2})$$

$$\sim 0.4 \quad \text{for } \lambda \leq 1.8a, \quad (\text{A3})$$

and the functional forms of RATs from the AMO, we can write RAT components as following

$$Q_{e_1}(\Theta, \beta, \Phi = 0) = \frac{|Q_{\Gamma}| q^{max}}{\sqrt{(q^{max})^2 + 1}} \frac{q_{e_1}(\Theta, \beta, \Phi = 0)}{q_{e_1}^{max}}, \quad (\text{A4})$$

$$Q_{e_2}(\Theta, \beta, \Phi = 0) = \frac{|Q_{\Gamma}|}{\sqrt{(q^{max})^2 + 1}} \frac{q_{e_2}(\Theta, \beta, \Phi = 0)}{q_{e_2}^{max}}, \quad (\text{A5})$$

$$Q_{e_3}(\Theta, \beta, \Phi = 0) = \frac{|Q_{\Gamma}| q^{max}}{\sqrt{(q^{max})^2 + 1}} \frac{q_{e_3}(\Theta, \beta, \Phi = 0)}{q_{e_3}^{max}}, \quad (\text{A6})$$

where

$$q_{e_1}(\Theta, \beta, \Phi = 0) = -\frac{4l_1}{\lambda} C \left(n_1 n_2 \cos^2 \Theta + \frac{n_1^2}{2} \cos \beta \sin 2\Theta - \frac{n_2^2}{2} \cos \beta \sin 2\Theta - n_1 n_2 \sin^2 \Theta \cos^2 \beta \right), \quad (\text{A7})$$

$$q_{e_2}(\Theta, \beta, \Phi = 0) = \frac{4l_1}{\lambda} C \left(n_1^2 \cos \beta \cos^2 \Theta - \frac{n_1 n_2}{2} \cos^2 \beta \sin 2\Theta - \frac{n_1 n_2}{2} \sin 2\Theta + n_2^2 \cos \beta \sin^2 \Theta \right), \quad (\text{A8})$$

$$q_{e_3}(\Theta, \beta, \Phi = 0) = \frac{4l_1}{\lambda} C n_1 \sin \beta [n_1 \cos \Theta - n_2 \cos \beta \sin \Theta] + \left(\frac{b}{l_2}\right)^2 \frac{2ea}{\lambda} (s^2 - 1) K(\Theta) \sin 2\Theta, \quad (\text{A9})$$

with $q_{e_j}^{max} = \max \langle q_{e_j}(\Theta, \beta, \Phi = 0) \rangle_{\beta}$ for $j = 1, 2$ and 3 . The ratio of torque components is then defined by

$$q^{max} = \frac{\max \langle Q_{e_1}(\Theta, \beta, \Phi = 0) \rangle_{\beta}}{\max \langle Q_{e_2}(\Theta, \beta, \Phi = 0) \rangle_{\beta}}. \quad (\text{A10})$$

In equations (A7)-(A9), C is a function defined as

$$C = |n_1 \cos \Theta - n_2 \sin \Theta \cos \beta|, \quad (\text{A11})$$

where Θ is the angle between the axis of maximum moment of inertia \mathbf{a}_1 and the radiation direction \mathbf{k} , β is the angle describing the rotation of the grain about \mathbf{a}_1 (see Fig. 1 lower); $n_1 = -\sin \alpha, n_2 = \cos \alpha$ are components of the normal vector of the mirror tilted by an angle α in the grain coordinate system, a, b are minor and major semi-axes of the spheroid, $s = a/b < 1$ and e is the eccentricity of the spheroid, l_1 is the distance from the mirror to the spheroid, and l_2 is the size of the squared mirror; $K(\Theta)$ is the fitting function (see also LH07a). The second term of equation (A9) represents the torque due to the spheroid. Assuming $l_1 \sim \lambda$ and $b, a \sim l_2 \ll l_1$, then this term is subdominant compared to the first term (see Fig. 2). Thus, we disregard it in our calculations.

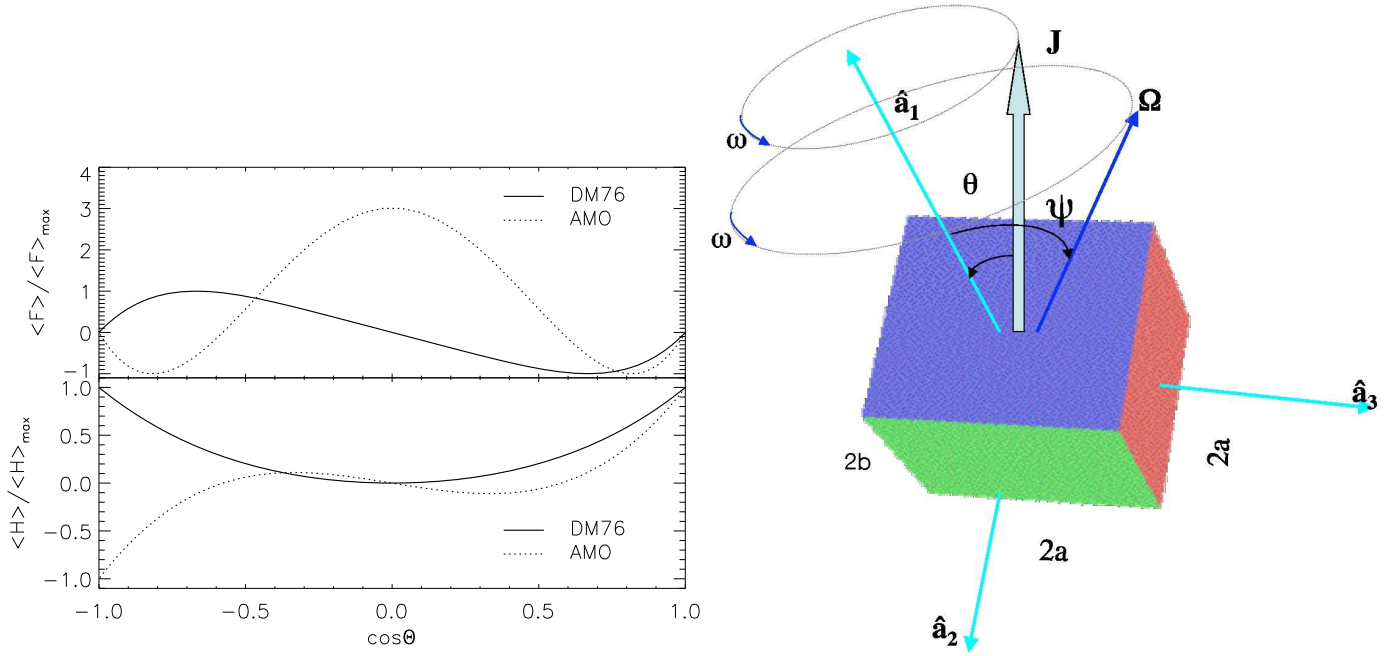


FIG. 18.— *Upper panel:* Comparison of RATs components for AMO and DM76. Θ is the angle between the axis of maximum moment of inertia (shortest) with the radiation in AMO, and is the angle between the twisted axis (longest axis) and radiation for DM76. Stationary points $\Theta = 0, \pi$ appear in both models, but the form of torques are different. $\langle F \rangle$ is symmetric for the AMO, but not for SM76, also in DM76, $\langle H \rangle$ is symmetric instead. *Lower panel:* A brick grain adopted in calculations for internal relaxation timescale.

Our calculations for the alignment in the presence of thermal fluctuations showed that the AMO can reproduce the alignment property with low- J as found with RATs obtained by DDSCAT when q_{e1} is modified to (see HL08a)

$$q_{e1}(\Theta, \beta, \Phi = 0) = -\frac{4I_1}{\lambda} C \left(n_1 n_2 \frac{[3\cos^2\Theta - 1]}{2} + \frac{n_1^2}{2} \cos\beta \sin 2\Theta - \frac{n_2^2}{2} \cos\beta \sin 2\Theta - n_1 n_2 \cos 2\beta \right). \quad (\text{A12})$$

This modification can arise from the imperfect scattering and/or the absorption effect by the mirror (LH07a). Also, the results in LH07a remain unchanged because the averaging over β for the last term goes to zero.

We adopt the AMO with $\alpha = 45^\circ$ in this paper, unless mentioned otherwise. We also assume the amplitude of Q_{e3} is comparable to that of Q_{e1} and Q_{e2} .

RATs at a precession angle Φ (see Fig. 1lower) can be derived from RATs at $\Phi = 0$ using the coordinate system transformation, as follows:

$$Q_{e1}(\Theta, \beta, \Phi) = Q_{e1}(\Theta, \beta, \Phi = 0), \quad (\text{A13})$$

$$Q_{e2}(\Theta, \beta, \Phi) = Q_{e2}(\Theta, \beta, \Phi = 0) \cos\Phi + Q_{e3}(\Theta, \beta, \Phi = 0) \sin\Phi, \quad (\text{A14})$$

$$Q_{e3}(\Theta, \beta, \Phi) = Q_{e2}(\Theta, \beta, \Phi = 0) \sin\Phi - Q_{e3}(\Theta, \beta, \Phi = 0) \cos\Phi. \quad (\text{A15})$$

AMO versus the model of Dolginov & Mytrophanov 1976

Figure 18 shows the comparison of the RAT components for the AMO and RATs obtained for the twisted spheroid from Dolginov & Mytrophanov (1976). It can be seen that the torques are radically different. According to LH07a, the AMO corresponds to calculations of torques for irregular grains, thus we can conclude that the model in Dolginov & Mytrophanov (1976) does not represent adequately RATs.

DYNAMICAL EQUATIONS FOR IRREGULAR GRAINS

For irregular grains, we define a parameter which is constant during the free-torque motion:

$$p = \frac{2I_1 E}{J^2}, \quad (\text{B1})$$

where E is the total energy, I_1 is the inertia moment along the principal axis \mathbf{a}_1 and J is the value of angular momentum. Since both J and E are conserved during the torque-free motion, p is accordingly conserved. The evolution of p in time due to external torques is then

$$\frac{dp}{dt} = \frac{1}{J^2} \left(2I_1 \frac{dE}{dt} J - 2I_1 E \frac{dJ}{dt} \right) \quad (\text{B2})$$

The energy of the grains varies as

$$\frac{dE}{dt} = \left(\mathbf{J} \cdot \frac{d\boldsymbol{\omega}}{dt} + \Gamma \cdot \boldsymbol{\omega} \right) \quad (\text{B3})$$

The first term describes the energy dissipation due to the Barnett and nuclear relaxation. The second terms represents the effect of external torques on the grain rotational energy. This equation differs from that in WD03 by a factor of 2. We consider here only RATs, so $\Gamma = \Gamma_{rad} = MQ_{\Gamma}$.

Substituting dE/dt into equation (B2), we get

$$\frac{dp}{dt} = \frac{1}{J^2} \left[I_1 \left(\mathbf{J} \cdot \frac{d\boldsymbol{\omega}}{dt} + \Gamma \cdot \boldsymbol{\omega} \right) - p \mathbf{J} \cdot \Gamma \right]. \quad (\text{B4})$$

Averaging equation (B4) over the torque-free motion, we obtain

$$\frac{J^2 dp}{dt} = MI_1 \langle Q_{\omega} \rangle - pJ \frac{dJ}{dt} - \frac{(p-1)}{t_{int}} \left(\frac{1-pI_3/I_1}{1-I_3/I_1} \right), \quad (\text{B5})$$

where we used $\Gamma = d\mathbf{J}/dt$, and

$$Q_{\omega} = \mathbf{Q}_{\Gamma} \cdot \boldsymbol{\omega} = Q_{a_1} \omega_1 + Q_{a_2} \omega_2 + Q_{a_3} \omega_3. \quad (\text{B6})$$

Here ω_i for $i=1,2$ and 3 corresponds to the components of angular velocity along three grain axes $\mathbf{a}_1, \mathbf{a}_2$ and \mathbf{a}_3 .

RAT ALIGNMENT INDUCED BY A SINGLE COMPONENT FOR THE SPHEROIDAL AMO

We study first the alignment with high- J attractor. For this purpose, we consider the alignment by the first component Q_{e_1} , which is shown to produce the alignment with high- J attractor (see LH07a). With this simplification, we can obtain the analytical results for the motion. According to equation (31) in HL08a, the averaged value of Q_{e_1} over torque-free motion, and fast Larmor precession is given by

$$\langle Q_{e_1} \rangle_{\phi} = Q_{e_1}^{max} \left(3 \cos^2 \xi \cos^2 \theta + \frac{3 \sin^2 \xi \sin^2 \theta}{2} - 1 \right), \quad (\text{C1})$$

$$\langle Q_{a_1} \rangle_{\phi} = Q_{e_1}^{max} \cos \theta \cos \xi \left(-1 + 3 \cos^2 \xi \cos^2 \theta + \frac{9}{2} \sin^2 \xi \sin^2 \theta \right). \quad (\text{C2})$$

The aligning and spin-up torque components are then

$$\langle F \rangle_{\phi} = -\langle Q_{e_1} \rangle_{\phi} \sin \xi, \quad (\text{C3})$$

$$\langle H \rangle_{\phi} = \langle Q_{e_1} \rangle_{\phi} \cos \xi. \quad (\text{C4})$$

It can be seen that the torque components are functions of two alignment angles θ and ξ .

Let us investigate the property of these stationary points. Consider first the stationary points $\xi = \pi$ and $\theta = 90^\circ$. Equation (C4) shows that $\langle H \rangle_{\phi} = \langle Q_{e_1}^{max} \rangle^2 > 0$ because $\langle Q_{e_1} \rangle = -Q_{e_1}^{max}$. In addition, the first derivative of $\langle F \rangle_{\phi} < 0$ (see eq. C3). Therefore, $\xi = \pi$ is a high- J attractor with $\theta = 90^\circ$. Moreover, the stationary point $\xi = 0, \theta = 0$ is still a high- J attractor because $\langle F' \rangle_{\phi} / \langle H \rangle_{\phi} < 0$. This indicates that in the absence of internal dissipation, the alignment occurs in two types: the longest axis parallel and perpendicular to the magnetic field. The former is consistent with the Davis-Greenstein prediction, i.e., ‘‘right’’ alignment, while the later provides ‘‘wrong’’ alignment (see LH07a).

The trajectory map in Figure 19 for the alignment by one component Q_{e_1} exhibits two high- J attractors A and D, as expected. In addition, there are two repellers B and C. The final state of grains depends on their initial angles ξ_0 . For instance, grains with initial angles $|\cos \xi_0| > 0.6$ are aligned on A and D, but grains with $|\cos \xi_0| < 0.6$ are constrained within two repellers B and C, and finally damped by gas friction.

The lower panel represents the evolution of θ and ξ as functions of time for few grains with $\cos \xi_0 < -0.8$. It can be seen that the angular momentum of these grains are perfectly aligned with respect to the magnetic field, but the shortest axis \mathbf{a}_1 is nearly perpendicular to \mathbf{J} , corresponding to ‘‘wrong’’ internal alignment.

TRANSFORMATION OF COORDINATE SYSTEM

To find the torques in the lab system (\mathbf{e}_i) when the radiation direction \mathbf{k} varies, we need to implement the coordinate transformation from the system $kk_x k_y$ to \mathbf{e}_i (see Fig. 13). We assume that the magnetic field is directed along \mathbf{e}_1 , then the $\mathbf{k}_z = \mathbf{k}$, and \mathbf{k}_y lies in the plane \mathbf{B}, \mathbf{k} . Thus, \mathbf{k}_x is perpendicular to the plane \mathbf{k}, \mathbf{k}_y . Therefore, the coordinate system $\mathbf{k}, \mathbf{k}_x, \mathbf{k}_y$ acts as the system \mathbf{e}_i in Figure 1.

Denote Q_k be torques components in the k-system, we need to know the torque components in the lab system. The transformation from k-system to \mathbf{e}_i -system is carried out by three rotations with three Euler angles.

Following Figure 13, we have

$$\mathbf{e}_1^X = \mathbf{e}_1 \cos \chi + \mathbf{e}_2 \sin \chi, \quad (\text{D1})$$

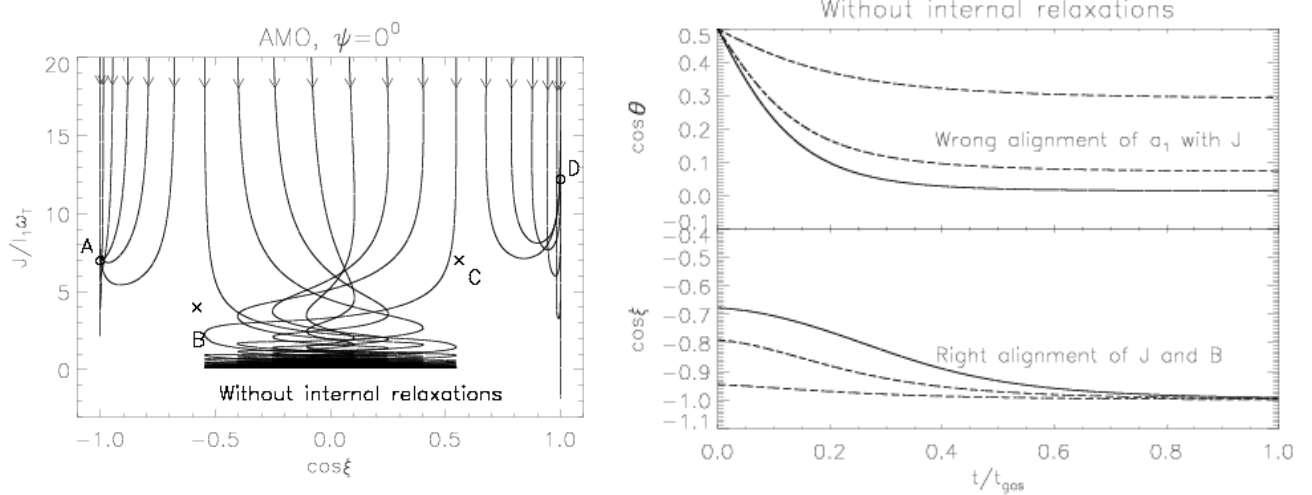


FIG. 19.— *Upper panel:* RAT alignment by Q_{e1} , in the absence of internal relaxation. A and D denoted by circles are high- J attractors, and C and D denoted by crosses are repellers. The alignment at A corresponds to $\mathbf{a}_1 \perp \mathbf{B}$, and $\mathbf{a}_1 \parallel \mathbf{B}$ for the alignment at D. *Lower panel:* Evolution of θ and ξ for a few grains with $\cos \xi_0 < -0.8$ as functions of time.

$$\mathbf{e}_1^X = -\mathbf{e}_1 \sin \chi + \mathbf{e}_2 \cos \chi, \quad (\text{D2})$$

$$\mathbf{e}_3^X = \mathbf{e}_3 \quad (\text{D3})$$

The radiation direction \mathbf{k} is determined by two angles ψ_k and ϕ_k in the lab system, we have the coordinate transformation from \mathbf{k} -system to \mathbf{d} -system:

$$\mathbf{e}_1^0 = \mathbf{e}_1^X \cos \psi_k + \mathbf{e}_2^X \sin \psi_k \cos \phi_k + \mathbf{e}_3^X \sin \psi_k \sin \phi_k \quad (\text{D4})$$

$$\mathbf{e}_2^0 = -\mathbf{e}_1^X \sin \psi_k + \mathbf{e}_2^X \cos \psi_k \cos \phi_k + \mathbf{e}_3^X \cos \psi_k \sin \phi_k \quad (\text{D5})$$

$$\mathbf{e}_3^0 = \mathbf{e}_2^X \sin \phi_k + \mathbf{e}_3^X \cos \phi_k^X \quad (\text{D6})$$

Assuming that \mathbf{a}_1 is parallel to \mathbf{J} , which is described by ξ, ϕ in the lab system, then we have

$$\mathbf{a}_1 = \mathbf{e}_1 \cos \xi + \mathbf{e}_2 \sin \xi \cos \phi + \mathbf{e}_3 \sin \xi \sin \phi \quad (\text{D7})$$

$$\mathbf{a}_2 = -\mathbf{e}_1 \sin \xi + \mathbf{e}_2 \cos \xi \cos \phi + \mathbf{e}_3 \cos \xi \sin \phi, \quad (\text{D8})$$

$$(\text{D9})$$

We can find the angles Θ, Φ and β in the \mathbf{e}_i^0 system:

$$\cos \Theta = \mathbf{e}_1^0 \cdot \mathbf{a}_1, \quad (\text{D10})$$

$$\tan \frac{\Phi}{2} = \frac{\sin \Theta - \mathbf{a}_1 \cdot \mathbf{e}_2^0}{\mathbf{a}_1 \cdot \mathbf{e}_3^0} \quad (\text{D11})$$

$$\beta = 2 \tan^{-1} \left(\frac{\sin \Theta + \mathbf{a}_2 \cdot \mathbf{e}_2^0}{\sin \Theta (\mathbf{a}_2 \cdot \mathbf{e}_3^0 \cos \Phi - \mathbf{a}_2 \cdot \mathbf{e}_2^0 \sin \Phi)} \right), \quad (\text{D12})$$

By substituting equations (D4)-(D6) and (D7) and (D8) into (D10) and (D12), we obtain the angles Θ, Φ and β , the torques Q_{ei}^0 are interpolated. Finally, we find the corresponding torques, $Q_{ei}(\xi, \phi)$ by coordinate transformation:

$$Q_{ei} = C_{ij}^T B_{jk}^T Q_{ek}^0, \quad (\text{D13})$$

Here matrices C^T, B^T are tranposal matrices of C and B , inferred from the equations (D10)-(D12) and (A4)-(B1) following

$$\mathbf{e}_i^X = \mathbf{C}_{ij} \mathbf{e}_j, \quad (\text{D14})$$

$$\mathbf{e}_i^0 = \mathbf{B}_{ij} \mathbf{e}_j^X. \quad (\text{D15})$$